ELECTROOPTIC LIGHT MODULATOR WITH IMPROVED RESPONSE

LINEARITY USING OPTICAL FEEDBACK

A Dissertation

by

APICHAI BHATRANAND

Submitted to the Office of Graduate Studies of
Texas A&M University
in partial fulfillment of the requirements for the degree of

DOCTOR OF PHILOSOPHY

August 2004

Major Subject: Electrical Engineering

ELECTROOPTIC LIGHT MODULATOR WITH IMPROVED RESPONSE

LINEARITY USING OPTICAL FEEDBACK

A Dissertation

by

APICHAI BHATRANAND

Submitted to Texas A&M University
in partial fulfillment of the requirements
for the degree of

DOCTOR OF PHILOSOPHY

Approved as to style and content by:

Henry F. Taylor (Chair of Committee)	
Ohannes Eknoyan (Member)	Kai Chang (Member)
Donald R. Smith (Member)	Chanan Singh (Head of Department)

August 2004

Major Subject: Electrical Engineering

ABSTRACT

Electrooptic Light Modulator with Improved Response Linearity

Using Optical Feedback. (August 2004)

Apichai Bhatranand, B.S., Mahidol University;

M.E., Texas A&M University

Chair of Advisory Committee: Dr. Henry F. Taylor

The use of optical feedback for improving response linearity of electrooptic light modulators has been investigated. The modulator is configured as a straight channel waveguide flanked by electrodes in a lithium niobate (LiNbO$_3$) substrate. Light is coupled into the waveguide in both TE and TM polarizations, and a voltage applied across electrodes causes a relative phase shift between two polarization components. An output analyzer converts the phase modulation to intensity modulation. Optical feedback of light in both polarization modes results from reflection of light at the polished edges of the substrate.

Channel waveguides supporting a single guided mode for TE and TM polarizations were fabricated in x-cut LiNbO$_3$ substrates using titanium-indiffusion technique. The waveguides and modulators were characterized at a wavelength of 1.55 μm using a distributed feedback laser.

The modulators were driven with a sinusoidal voltage waveform. To minimize harmonics of the modulating frequency in the intensity output, the magnitude of the optical feedback and the substrate temperature were adjusted. The feedback level was

altered by applying refractive index-matching liquid to one or both ends of the waveguide at the edges of the crystal. It was found that a high degree of response linearity in the presence of feedback was achievable at certain substrate temperatures.

The spurious-free dynamic range (SFDR) relative to the noise floor was measured at different feedback levels and substrate temperatures in an effort to maximize the modulator response linearity. An SFDR of 68.04 dB, limited by third-order nonlinearity, was achieved by applying index-matching fluid to the input end of the substrate. This compares with an SFDR of 64.84 dB limited by second-order nonlinearity when index-matching fluid was applied at both ends of the substrate. By changing the temperature of the same substrate to adjust the phase shifts experienced by TE and TM polarizations, the SFDR with index-matching fluid at the input end increased to 71.83 dB, limited by third-order nonlinearity.

In tests at constant modulation depth, an improvement of as much as 9.6 dB in SFDR vs. the theoretical value for an interferometric modulator without feedback was achieved.

To My Family

ACKNOWLEDGMENTS

I would like to express my gratitude to my advisor and committee chair, Dr. H. F. Taylor, and to my committee member, Dr. O. Eknoyan, from the deepest place of my heart. I would never find words to thank them for their time, support, guidance, and encouragement throughout my education at Texas A&M University. Without them, this dissertation would not have been accomplished. I would like to thank the other committee members, Dr. K. Chang and Dr. D. R. Smith, for their time and concern by serving as my committee. I also thank Dr. S. DiMarco for once serving as my GCR.

To the current lab manager, Mr. R. A. Atkins, and former lab manager, Mr. C. Henderson, I truly appreciate their massive contributions throughout my work in the lab. I also thank Ms. L. Huval for her generous help in many ways. To my sponsor, the Royal Thai Government, I am grateful for financially supporting me. To my friends and colleagues, P. Tang, D. Gu, O. Kwon, N. Suphasan, R. Wang, H. Kuo, R. Kim,Y. Ping, and Y. Shin, for their friendship, advice, and support. I also thank all my Thai friends for making Aggieland such an awesome place.

Special thanks to Pong for being on my side throughout the ups and downs during my study. Finally, I gratefully thank my family for their love, support, and encouragement.

TABLE OF CONTENTS

TABLE OF CONTENTS (continued)

TABLE OF CONTENTS (continued)

LIST OF FIGURES

LIST OF FIGURES (continued)

FIGURE   Page

LIST OF TABLES

CHAPTER I

INTRODUCTION

Analog signal transmission over optical fibers is of considerable practical interest for application in cable television and in the transmission of radio frequency and microwave signals between antennas and remote locations. In such systems, an electrical signal modulates the intensity of an optical carrier in a transmitter, and the optical signal transmitted over a fiber is converted to an electrical signal in a receiver. For analog transmission, it is desired that the optical intensity be a linear function of the modulating electrical signal in order that the received electrical signal be a faithful reproduction of the modulating electrical signal in the transmitter. The uses of external optical modulators in conjunction with continuous wave (cw) laser light sources have been widely studied for use in analog links. Electro-absorption and electrooptic modulators are the leading candidates for use in wideband analog systems. Since electro-absorption modulators are very lossy, electrooptic modulators are more widely used.

Linearity of the dependence of transmitted optical power on modulating voltage is a key issue in external modulators for analog transmission. There are two conventional electrooptic modulators: the Mach-Zehnder interferometric type and the directional-coupler type [1]. Both have a nonlinear dependence of transmitted optical

_____

This thesis follows the style and format of *IEEE Journal of Lightwave Technology*.

power on applied voltage, which limits the spurious free dynamic range (SFDR) of the photonic link in which they are used by generating harmonics and intermodulation products. Generally, interferometric optical modulators are biased at the quadrature point to eliminate second harmonics of the modulating waveform, so that quasilinear operation is achieved over a narrow range of modulating phase shift. The dynamic range of a system that uses quadrature-biased modulation is limited by the third harmonic. The third order nonlinearities can be held within acceptable limits by restricting the optical modulation depth to few percents. Various optical modulator configurations with improved linearity have been proposed and demonstrated, including dual Mach-Zehnders [2],[3], cascaded Mach-Zehnders [4],[5], polarization-mixing [6], and modified directional coupler modulators [7]. These schemes have proven to be difficult to implement [8]. Some researchers suggest the predistortion of the electrical modulation signal [9] to compensate for the optical nonlinearity, but the degree of compensation using this technique is limited and the effectiveness of this method decreases with increasing bandwidth of the optical link.

A new design for electrooptic intensity modulators with improved linearity is described here. The modulator consists of a straight channel waveguide with electrodes for producing different voltage-dependent electrooptic phase shifts between TE and TM polarization mode. A linear analyzer placed at the output converts the phase modulation to intensity modulation. Analysis predicts an improvement in the linearity of response through optical feedback provided by the reflection of light at the polished edges of the crystal. The level of feedback can be adjusted by applying

index-matching liquid at the substrate-air interfaces at the ends of the waveguide. Another adjustable parameter to improve the linearity is the birefringence of the waveguide, which can be changed by varying the substrate temperature to adjust the phase shifts experienced by TE and TM modes in the absence of modulation. At certain temperatures, harmonics of a modulating frequency are reduced in comparison with those seen in modulators without optical feedback.

The primary objective of this research is to conduct experiments to verify and quantify the linearity improvement which might be achieved using this optical feedback approach in a simple straight channel waveguide configuration.

A brief theoretical review of principles upon which the modulator is based is given in Chapter II. The operation and analysis of the device are described in Chapter III. Chapter IV explains the device fabrication process. Experimental results are discussed in Chapter V. Concluding remarks are given in Chapter VI, and Chapter VII contains suggestions for future research in this area.

CHAPTER II

THEORETICAL REVIEW

In this chapter, a brief review of wave propagation properties and optical waveguides based on Maxwell's Equations is presented. Plane wave propagation in uniaxial crystals is described. The electrooptic effect and electrooptic modulation are explained, and the concept of spurious-free dynamic range is introduced.

A. Wave Propagation and Optical Waveguides

The wave propagation can be analyzed from these four equations known as Maxwell's equations:

$$\nabla \times \mathbf{E} = -\frac{\partial \mathbf{B}}{\partial t} \tag{2.1}$$

$$\nabla \times \mathbf{H} = \mathbf{J} + \frac{\partial \mathbf{D}}{\partial t} \tag{2.2}$$

$$\nabla \cdot \mathbf{D} = \rho \tag{2.3}$$

$$\nabla \cdot \mathbf{B} = 0 \tag{2.4}$$

where $\mathbf{E}$ represents electric field intensity vector (V/m), $\mathbf{H}$ represents magnetic field intensity vector (A/m), $\mathbf{D}$ is electric flux density (electric displacement) vector (C/m^2), $\mathbf{B}$ is magnetic flux density (magnetic displacement) vector (T), $\mathbf{J}$ is the density of free currents (A/m^2), and ρ is the volume density of free charges (C/m^2). For linear and isotropic media, $\mathbf{E}$ and $\mathbf{D}$ are related by the constitutive relation as

$$\mathbf{D} = \varepsilon_0 \mathbf{E} + \mathbf{P} = \varepsilon \mathbf{E} \tag{2.5}$$

$$\mathbf{P} = \varepsilon_0 \chi_e \mathbf{E} \tag{2.6}$$

where ε is the permittivity of the medium (F/m), ε_0 is the permittivity of free space, χ_e is the electric susceptibility of the medium (unitless) and $\mathbf{P}$ is the electric polarization (dipole moment per unit volume) of the medium. The constitutive relation for $\mathbf{B}$ and $\mathbf{H}$ in linear and isotropic media is

$$\mathbf{B} = \mu_0 (\mathbf{H} + \mathbf{M}) = \mu \mathbf{H} \tag{2.7}$$

where μ is the permeability of the medium (H/m), μ_0 is the permeability of free space, and $\mathbf{M}$ is the magnetic polarization (dipole moment per unit volume) of the medium. Assume the medium is non-magnetic homogeneous dielectric ($\mu = \mu_0, \varepsilon = \varepsilon_0 n^2$) and free of source ($\mathbf{J} = 0$ and $\rho = 0$), with the use of equation (2.5), (2.6) and (2.7), the equation (2.1) and (2.2) become:

$$\nabla \times \mathbf{E} = -\mu \frac{\partial \mathbf{H}}{\partial t} \tag{2.8}$$

$$\nabla \times \mathbf{H} = \varepsilon \frac{\partial \mathbf{E}}{\partial t} = n^2 \varepsilon_0 \frac{\partial \mathbf{E}}{\partial t} \tag{2.9}$$

where $c = \dfrac{1}{\sqrt{\varepsilon_0 \mu_0}}$ is the light velocity in free space , and the reflective index, $n = \sqrt{\varepsilon_r \mu_r}$. Taking the curl of equation (2.8) and combining it with equation (2.9), where we use $\mathbf{A} \times \mathbf{B} \times \mathbf{C} \equiv \mathbf{B}(\mathbf{A} \cdot \mathbf{C}) - \mathbf{C}(\mathbf{A} \cdot \mathbf{B})$, and the help from equation (2.3) and (2.4) yields

$$\nabla^2 \mathbf{E} - \frac{n^2}{c^2}\frac{\partial^2 \mathbf{E}}{\partial t} = 0 \tag{2.10}$$

Generally, the electric field $\mathbf{E}$, can be expressed in time variation form as

$$\mathbf{E}(r,t) = \mathbf{E}(r)e^{j\omega t} \tag{2.11}$$

Since $\dfrac{\partial}{\partial t} = j\omega$, an equation (2.10) can be written in the simple form of

$$\nabla^2 \mathbf{E}(r) + k_0^2 n^2 \mathbf{E}(r) = 0 \tag{2.12}$$

where the free space propagation constant of light $k_0 = \dfrac{\omega}{c}$, and the angular frequency,

$\omega = \dfrac{2\pi c}{\lambda}$. Suppose that the plane wave propagates along z-direction with the

propagation constant β, the form of the field is taken as

$$\mathbf{E}(r,t) = \mathbf{E}(x, y)e^{j(\omega t - \beta z)} \tag{2.13}$$

so that equation (2.12) becomes,

$$\left(\frac{\partial^2}{\partial x^2} + \frac{\partial^2}{\partial y^2}\right)\mathbf{E}(x, y) + \left(k_0^2 n^2 - \beta^2\right)\mathbf{E}(x, y) = 0 \tag{2.14}$$

The behavior of dielectric waveguides can be explained with the help of a planar (slab) model with no variation of refractive index or electric field in one dimension. A channel waveguide, in which the dimensions are finite in both x- and y- direction, approaches the behavior of the planar guide when one dimension is considerably larger than the other. Most of the phenomena of interest are only modified in a simple quantitative way when going from a planar to a channel waveguide [10].

Region 1 n_1 0

Region 2 n_2

                                            -t

Region 3 n_3
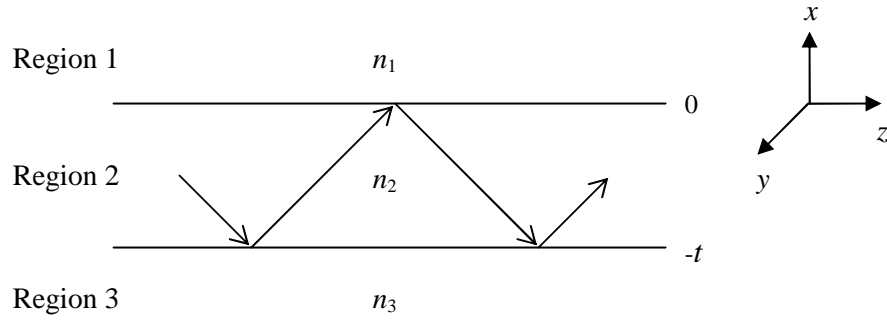
Figure 2.1 Planar or slab dielectric waveguide ($\partial/\partial y = 0$)

Considering the planar dielectric waveguide, with no variation in *y*-axis, as shown in Figure 2.1, equation (2.14) for the three regions becomes:

$$\text{Region 1: } \frac{d^2}{dx^2}E(x) + \left(k_0^2 n_1^2 - \beta^2\right)E(x) = 0$$

$$\text{Region 2: } \frac{d^2}{dx^2}E(x) + \left(k_0^2 n_2^2 - \beta^2\right)E(x) = 0 \qquad (2.15)$$

$$\text{Region3: } \frac{d^2}{dx^2}E(x) + \left(k_0^2 n_3^2 - \beta^2\right)E(x) = 0$$

where $E(x)$ is a Cartesian component of $\mathbf{E}(x)$.

Solution of equation (2.15) can be considered as a function of the propagation constant β at a fixed frequency ω. Assume that $n_2 > n_3 > n_1$ for $\beta > k_0\, n_2$, it follows directly from equation (2.15) that $(1/E)(\partial^2 E/\partial x^2) > 0$ everywhere which shows that the electric field $E(x)$ is exponential in all three regions of the waveguide in Figure 2.1. Because of the need to match both $E(x)$ and its derivatives at the two interfaces, the field increases without bound away from the waveguide, so that in this case the solution is unrealistic and does not correspond to a real wave. For $k_0\, n_3 < \beta < k_0\, n_2$, it

follows from equation (2.15) that the solution is sinusoidal in region 2 because of $(1/E)(\partial^2 E/\partial x^2) < 0$, but it is exponential in region 1 and 3 due to $(1/E)(\partial^2 E/\partial x^2) > 0$ as previous case. It is possible to have $E(x)$ satisfy the boundary conditions in the highest index of refraction region (region 2) and decay exponentially in the outer regions (region 1 and 3) shown in Figure 2.2. The energy carried by these modes is confined to the vicinity of the guiding region, and they are called *confined* or *guided* modes.
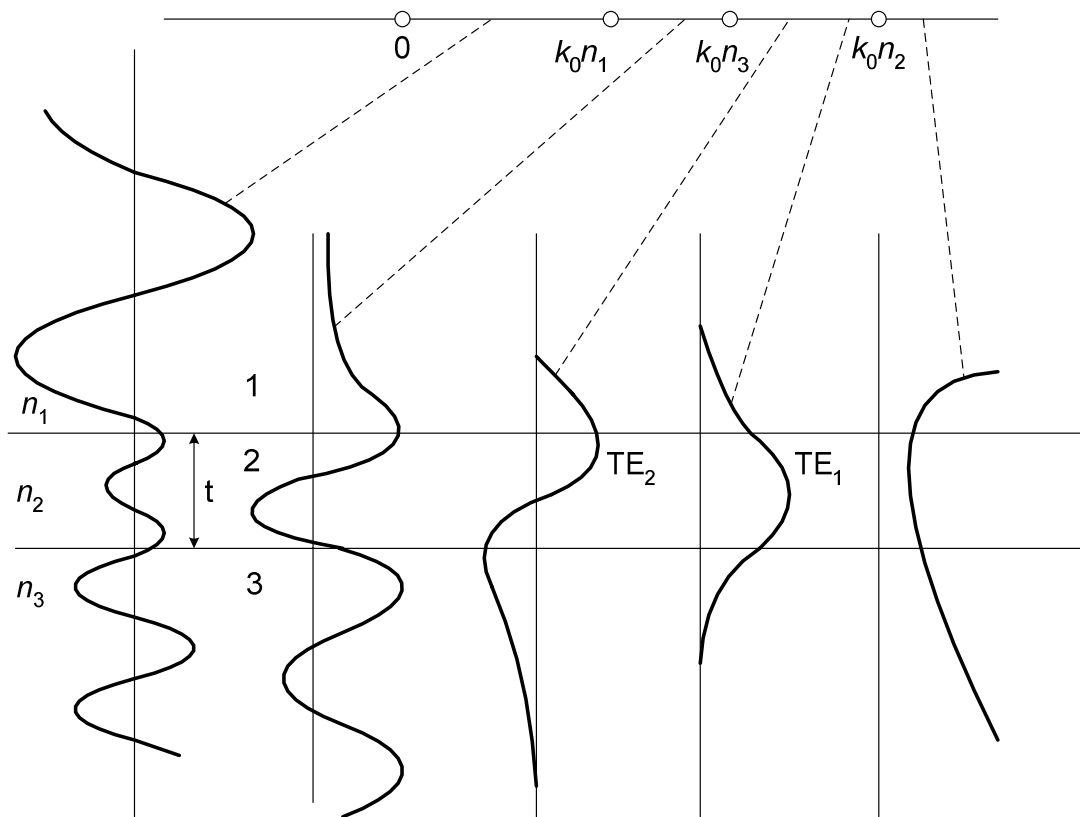
Figure 2.2 Wave field distributions of the waveguide shown in Figure 2.1 corresponding to the different value of β

For another case in which $k_0\, n_1 < \beta < k_0\, n_3$, the solutions for $E(x)$ are sinusoidal in region 2 and 3 and exponentially decaying in region 1. These modes are called *substrate radiation* mode. For the final case of $0 < \beta < k_0\, n_1$, the solution of $E(x)$ is sinusoidal in all three regions, so that modes in this cases are called *radiation* modes of waveguides.

From this analysis, confined or guided modes are possible only when $n_2 > n_1$, n_3; that is, the middle layer must have the largest index of refraction.

Generally, the planar waveguide shown in Figure 2.1 can support a finite number of guided modes. Those modes can be divided into two groups with mutually orthogonal polarization states. One consists of the fields E_y, H_x, and H_z and is called the transverse electric (TE) mode because the electric field is transverse to the propagation direction; i. e., there is no E_z component. The other is called transverse magnetic (TM) mode with fields H_y, E_x, and E_z.

From Figure 2.1, considering the TE mode case, light is traveling in the z-direction and polarized in the y-direction with the field components as

$$\mathbf{E}(\mathbf{r},t) = E_y(x)e^{i(\omega t - \beta z)}.\hat{a}_y \tag{2.16}$$

$$H_x = -\frac{\beta}{\omega\mu}E_y$$

$$H_z = -\frac{1}{j\omega\mu}\frac{\partial E_y}{\partial x} \tag{2.17}$$

From equation (2.15), the field solutions can be written in the form

$$E_y(x) = \begin{cases} Ce^{-qx} & \text{(Region 1)} \\ C\left[\cos(hx) - \dfrac{q}{h}\sin(hx)\right] & \text{(Region 2)} \\ C\left[\cos(ht) + \dfrac{q}{h}\sin(ht)\right]e^{p(x+t)} & \text{(Region 3)} \end{cases}$$
(2.18)

where C is arbitrary constant, t is the thickness of the planar waveguide, and

$q = \sqrt{\beta^2 - k_0^2 n_1^2}$, $h = \sqrt{k_0^2 n_2^2 - \beta^2}$, $p = \sqrt{\beta^2 - k_0^2 n_3^2}$. Apply the boundary condition that

the tangential field components E_y and H_z be continuous across the interfaces at both x

$= 0$ and $x = -t$, this yields the relationship

$$\tan(ht) = \frac{p+q}{(h - \dfrac{q}{h}p)}$$
(2.19)

This is called the characteristic equation for TE mode.

In case of TM modes, a similar approach is applied to that used above for the

TE modes.   The field components are

$$\mathbf{H}(\mathbf{r},t) = H_y(x)e^{i(\omega t - \beta z)}.\hat{a}_y$$
(2.20)

$$E_x = \frac{\beta}{\omega \varepsilon_0 n^2} H_y$$

$$E_z = \frac{1}{j\omega \varepsilon_0 n^2}\frac{\partial H_y}{\partial x}$$
(2.21)

Solving for the field solutions of $H_y(x)$ and applying the boundary condition in

a same manner as for the TE mode leads to the characteristic equation for TM mode

given by

$$\tan(ht) = \frac{\left(\dfrac{n_2}{n_1}\right)^2 q + \left(\dfrac{n_2}{n_3}\right)^2 p}{h - \left(\dfrac{n_2^2}{n_1 n_3}\right)\dfrac{pq}{h}} \qquad (2.22)$$

The characteristic equation is sometimes called an eigenvalue equation since it is used to find the allowed eigenvalues β for the guided modes. These values of β identify the number of allowed modes in that waveguide. For guided wave optoelectronics, the single mode waveguide is desired for most applications. That means only the lowest order mode, called the fundamental mode, is supported by the waveguide.

B. Optical Indicatrix in Uniaxial Crystals

If the medium is isotropic, the polarization in the material is parallel to the electric field and related to it by a constant electric susceptibility that is independent of the direction along which the field is applied as shown in equation (2.6). However, in case of anisotropic media, the electric susceptibility is no longer a constant; therefore, the polarization will depend in its magnitude and direction on the direction of the electric field as

$$\mathbf{P} = \varepsilon_0 \tilde{\chi}_e \mathbf{E} \qquad (2.23)$$

where $\tilde{\chi}_e$ is the 3×3 electric susceptibility tensor. To simplify the analysis, the reference coordinate can be chosen to be along the principal axes of the crystal, so that all off-diagonal components of the electric susceptibility tensor are zero. From

equation (2.5) and (2.23) with the use of diagonal $\tilde{\chi}_e$, the permittivity of the medium

can be yielded as

$$\tilde{\varepsilon} = \begin{bmatrix} \varepsilon_{11} & 0 & 0 \\ 0 & \varepsilon_{22} & 0 \\ 0 & 0 & \varepsilon_{33} \end{bmatrix} = \varepsilon_0 \begin{bmatrix} n_x^2 & 0 & 0 \\ 0 & n_y^2 & 0 \\ 0 & 0 & n_z^2 \end{bmatrix} \qquad (2.24)$$

where ε_{11}, ε_{22}, ε_{33} are called principal permittivities. It follows that from equation

(2.5) that the relationship of **E** and **D** can be rewritten as

$$\mathbf{D} = \begin{bmatrix} D_x \\ D_y \\ D_z \end{bmatrix} = \begin{bmatrix} \varepsilon_{11} & 0 & 0 \\ 0 & \varepsilon_{22} & 0 \\ 0 & 0 & \varepsilon_{33} \end{bmatrix} \begin{bmatrix} E_x \\ E_y \\ E_z \end{bmatrix} = \tilde{\varepsilon}\mathbf{E} \qquad (2.25)$$

Optical properties of crystals are determined by their crystal structures. There are 3

types of the mediums depending on the symmetry. The first one, so-called cubic

crystal, is optically *isotropic* when $n_x = n_y = n_z$. In crystals belonging to tetragonal,

trigonal, and hexagonal systems, the index ellipsoid is rotationary symmetrical with

respect to the *z*-axis, which is also called the optic axis. Such crystals, such as LiNbO$_3$

or LiTaO$_3$, are optically *uniaxial* where $n_x = n_y \neq n_z$. The last group of materials with

triclinic, monoclinic, or orthorhombic symmetry, where $n_x \neq n_y \neq n_z$, are referred to as

biaxial crystals [11].

The stored electric energy density in the crystal is given by

$$U_e = \frac{1}{2}\mathbf{E}\cdot\mathbf{D} \qquad (2.26)$$

Then substitute equation (2.25) into equation (2.26) yields

$$U_e = \frac{1}{2}\left[\frac{D_x^2}{\varepsilon_{11}} + \frac{D_y^2}{\varepsilon_{22}} + \frac{D_z^2}{\varepsilon_{33}}\right] \qquad (2.27)$$

Replacing the defined quantities; $x = D_x / \sqrt{2\varepsilon_0 U_e}$, $y = D_y / \sqrt{2\varepsilon_0 U_e}$, $z = D_z / \sqrt{2\varepsilon_0 U_e}$

with the use of equation (2.24) into equation (2.27). The equation (2.27) is reduced to

$$\frac{x^2}{n_x^2} + \frac{y^2}{n_y^2} + \frac{z^2}{n_z^2} = 1 \qquad (2.28)$$

Equation (2.28) represents an index ellipsoid or indicatrix with the principal axes x, y, and z.
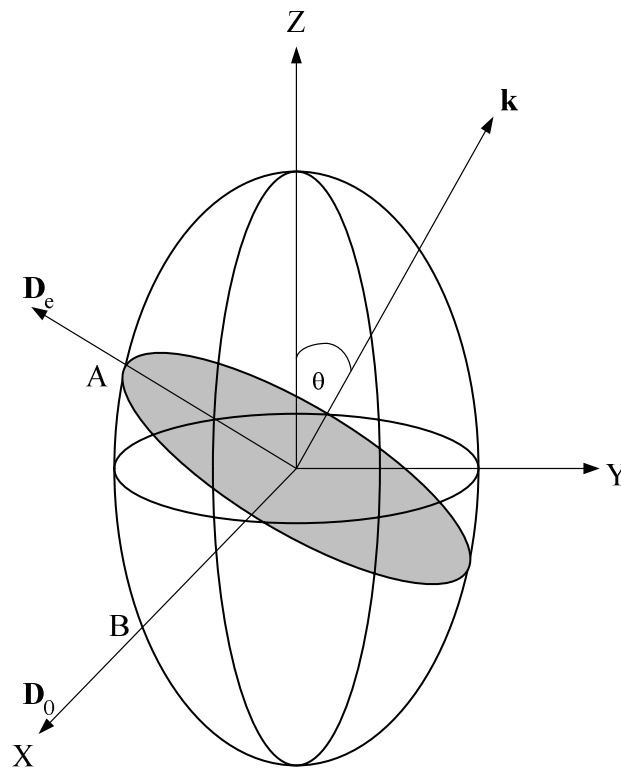
Figure 2.3 Index ellipsoid of uniaxial crystals

Consider light propagation in uniaxial crystals where $n_x = n_y = n_0$, $n_z = n_e$, and $n_0 > n_e$. The index ellipsoid of uniaxial crystals is shown in Figure 2.3, where **k** denotes the arbitrary direction of propagation vector making an angle θ with respect to the z-axis. Because the index ellipsoid is rotationary symmetrical with respect to the *z*-axis, the projection of **k** on the *x-y* plane can be chosen to coincide with the *y*-axis without loss of generality. The intersection ellipse of the plane normal to **k** with the ellipsoid is shaded as shown in Figure 2.3. In this situation, there are two orthogonal polarizations allowed parallel to the major and minor axes of the ellipse. One allowed polarization, **D**$_0$, along the OB direction, always see the refractive index n_0, which is independent of the angle θ. This is referred to as an *ordinary* wave. The other allowed polarization, **D**$_e$, parallel to the OA direction, sees the index $n_e(\theta)$, that depends on the angle θ. This is said to be an *extraordinary* wave. The index of extraordinary wave is equal to the length of OA in Figure 2.3, which is given by

$$
\begin{aligned}
n_e^2(\theta) &= y^2 + z^2 \\
y &= n_e(\theta)\cos\theta \\
z &= n_e(\theta)\sin\theta
\end{aligned}
\tag{2.29}
$$

Substituting equation (2.29) into equation (2.28) yields,

$$
n_e(\theta) = \frac{n_0 n_e}{\sqrt{n_e^2 \cos^2\theta + n_0^2 \sin^2\theta}}
\tag{2.30}
$$

From equation (2.30), it shows that the refractive index of the extraordinary wave varies from $n_e(\theta) = n_0$ at $\theta = 0$ to $n_e(\theta) = n_e$ at $\theta = 90^\circ$. In particular, when $\theta = 0$, the uniaxial crystal will behave as if it is optically isotropic (both ordinary and

extraordinary see the index n_0); therefore, the z-axis of uniaxial crystals is called the optical axis [11].

C. Electrooptic Effect

In principle, a variety of external perturbation such as electric field, magnetic field, temperature, or pressure, can modify the optical properties such as the refractive index. In the electrooptic effect, applied electric fields are used to change the optical properties [12]. There are two kinds of electrooptic effects; linear and quadratic. The linear electrooptic effect, also called the *Pockels* effect, is the change in the indices of the ordinary and extraordinary rays proportional to an applied electric field. This electrooptic effect exists only in crystals without an inversion symmetry, such as $LiNbO_3$. Therefore, the induced index change depends on the polarity of the voltage applied to the crystal. For a crystal with inversion symmetry, the linear electrooptic effect can not exist, while the quadratic electrooptic effect, known as the *Kerr* effect, is observed, where the induced index change is proportional to the square of the applied electric field [11]. Since the linear electrooptic effect is used in most integrated optic devices because it can produce a much larger refractive index change with applied electric field, the discussion here will focus on the Pockels effect only.

Since the propagation characteristics of crystals are described by means of the index ellipsoid defined by equation (2.28), the effect of an electric field on the propagation is expressed most conveniently by giving the changes in the constants

$1/n_x^2$, $1/n_y^2$, $1/n_z^2$ of the index ellipsoid. In the presence of an applied electric field, the equation of the index ellipsoid is generally expressed by [10]

$$\left(\frac{1}{n^2}\right)_1 x^2 + \left(\frac{1}{n^2}\right)_2 y^2 + \left(\frac{1}{n^3}\right)_3 z^2 + 2\left(\frac{1}{n^2}\right)_4 yz + 2\left(\frac{1}{n^2}\right)_5 xz + 2\left(\frac{1}{n^2}\right)_6 xy = 1 \qquad (2.31)$$

These new coefficients can be written as

$$\left(\frac{1}{n^2}\right)_i = \begin{cases} \left(\frac{1}{n_j^2}\right) + \Delta\left(\frac{1}{n^2}\right)_i & ; i = 1, 2, 3 \\ 0 + \Delta\left(\frac{1}{n^2}\right)_i & ; i = 4, 5, 6 \end{cases} \qquad (2.32)$$

where in the summation over j using the convention $1 = x$, $2 = y$, and $3 = z$. The linear electrooptic index change due to an applied electric field $\mathbf{E}^e(E_x, E_y, E_z)$ is defined by

$$\Delta\left(\frac{1}{n^2}\right)_i = \sum_{j=1}^{3} r_{ij} E_j \qquad (2.33)$$

where E_j^e are components of the applied electric field, r_{ij} is the 6×3 electrooptic coefficient tensor. Equation (2.33) can be written in a matrix form as

$$
\begin{bmatrix}
\Delta\left(\dfrac{1}{n^2}\right)_1 \\[4pt]
\Delta\left(\dfrac{1}{n^2}\right)_2 \\[4pt]
\Delta\left(\dfrac{1}{n^2}\right)_3 \\[4pt]
\Delta\left(\dfrac{1}{n^2}\right)_4 \\[4pt]
\Delta\left(\dfrac{1}{n^2}\right)_5 \\[4pt]
\Delta\left(\dfrac{1}{n^2}\right)_6
\end{bmatrix}
=
\begin{bmatrix}
r_{11} & r_{12} & r_{13} \\
r_{21} & r_{22} & r_{23} \\
r_{31} & r_{32} & r_{33} \\
r_{41} & r_{42} & r_{43} \\
r_{51} & r_{52} & r_{53} \\
r_{61} & r_{62} & r_{63}
\end{bmatrix}
\cdot
\begin{bmatrix}
E_1 \\
E_2 \\
E_3
\end{bmatrix}
\tag{2.34}
$$

The value of r_{ij} depends on the crystal symmetry. In LiNbO$_3$, the electrooptic tensor is [11]

$$
r_{ij} =
\begin{bmatrix}
0 & -r_{22} & r_{13} \\
0 & r_{22} & r_{13} \\
0 & 0 & r_{33} \\
0 & r_{51} & 0 \\
r_{51} & 0 & 0 \\
-r_{22} & 0 & 0
\end{bmatrix}
\tag{2.35}
$$

where $r_{33} = 30.8 \times 10^{-12}$ m/V, $r_{13} = 8.6 \times 10^{-12}$ m/V, $r_{22} = 3.4 \times 10^{-12}$ m/V, and $r_{51} = 26 \times 10^{-12}$ m/V [13].

Most electrooptic guided-wave devices in LiNbO$_3$ utilize the r_{33} electrooptic coefficient [14]. If the electric field is applied to a LiNbO$_3$ crystal along the z-direction, from equations (2.31), (2.34), and (2.35) with the presence of an electric field $\mathbf{E}^e(0, 0, E_z)$, the equation of the index ellipsoid becomes

$$\left(\frac{1}{n_0^2}+r_{13}E_z\right)x^2+\left(\frac{1}{n_0^2}+r_{13}E_z\right)y^2+\left(\frac{1}{n_e^2}+r_{33}E_z\right)z^2=1 \qquad (2.36)$$

where there is no mixed term (terms with xy, xz, and yz) in the equation of the index ellipsoid, then the major axes of the ellipsoid coincide with the principal axes (x, y, and z axes), and as the crystal is uniaxial, thus $n_x = n_y = n_0$, $n_z = n_e$. According to equation (2.36), the new indices can be found as

$$\frac{1}{n_x^2}=\frac{1}{n_0^2}+r_{13}E_z$$
$$\frac{1}{n_y^2}=\frac{1}{n_0^2}+r_{13}E_z \qquad (2.37)$$
$$\frac{1}{n_z^2}=\frac{1}{n_e^2}+r_{33}E_z$$

Since the index changes are very small, the conditions, $\left|r_{13}n_0^2E_z\right| \ll 1$, and $\left|r_{33}n_e^2E_z\right| \ll 1$ are satisfied, thus equation (2.37) yields the new refractive indices as

$$n_x = n_0 - \frac{1}{2}n_0^3 r_{13}E_z$$
$$n_y = n_0 - \frac{1}{2}n_0^3 r_{13}E_z \qquad (2.38)$$
$$n_z = n_e - \frac{1}{2}n_e^3 r_{33}E_z$$

In case of the appearance of mixed terms in the equation of the index ellipsoid due to an applied electric field, the major axes of the ellipsoid are no longer parallel to the principal axes. It is necessary to find the directions and magnitudes of the new principle axes to be able to obtain new indices.

D. Electrooptic Modulator

Phase and intensity waveguide modulators which utilize electrooptically induced refractive index changes are described below.

Phase Modulator. There are several configurations of phase modulators depending application of the electric field. A conventional planar waveguide phase modulator is shown in Figure 2.4. The modulator is fabricated by placing planar electrodes on a straight waveguide on z-cut x-propagation LiNbO$_3$ crystal. To make use of the largest electrooptic coefficient r_{33}, an electric field $\mathbf{E}^e$ is applied along the optic axis (z-axis) while the light is also polarized along the optical axis. Using equation (2.38), the accumulated phase at output due to the light propagation along the crystal with an applied voltage $\mathbf{E}^e(0, 0, E_z)$ is

$$\varphi(l) = \varphi_0 + \Delta\varphi = k\left(n_e - \frac{1}{2}n_e^3 r_{33}E_z\right)l \tag{2.39}$$

where $k = \dfrac{2\pi}{\lambda}$ and l is the interaction length. The phase shift $\Delta\varphi$ can be found from equation (2.39) as

$$\Delta\varphi = -\left(\frac{\pi l}{\lambda}\right)n_e^3 r_{33}E_Z \tag{2.40}$$

Since an electric field $\mathbf{E}^e$ is obtained by applying a voltage $v(\text{t})$ with an amplitude of V across the crystal with a thickness d, then $E = \dfrac{V}{d}$, the equation (2.40) gives

$$\Delta\varphi = \left(\frac{\pi}{\lambda}\right)n_e^3 r_{33}\left(\frac{l}{d}\right)V \tag{2.41}$$
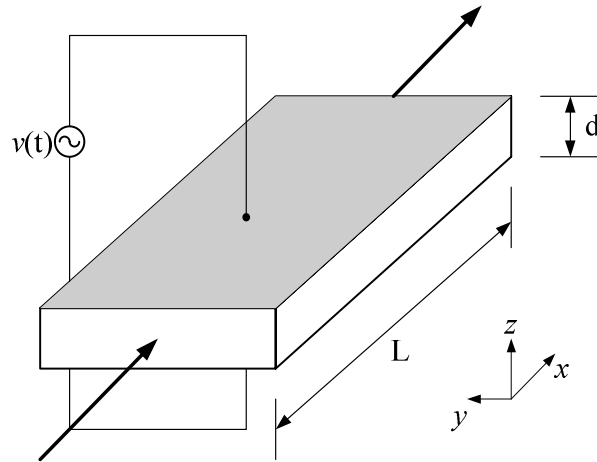
Figure 2.4 Transverse phase modulator

If the phase changes by π, equation (2.41) yields

$$V_\pi = \left(\frac{d}{l}\right)\frac{\lambda}{n_e^3 r_{33}} \tag{2.42}$$

where V_π is known as the half-wave voltage that is the applied voltage that makes the phase shift be π.

The goal in electrooptic modulator design is to obtain high modulation bandwidth with low drive voltage. Co-planar electrodes have been introduced on either side of the waveguide to reduce the applied voltage as shown in Figure 2.5.
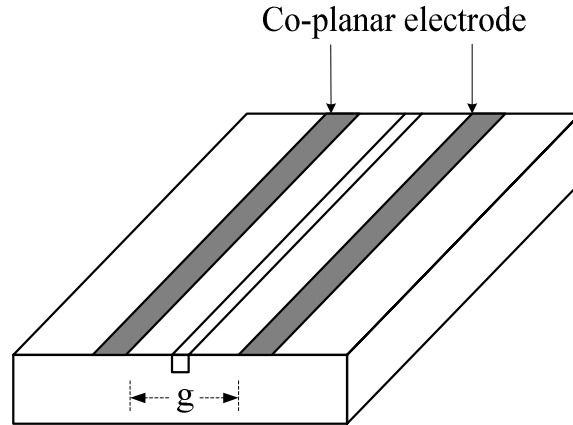
Figure 2.5 Co-planar electrodes with gap *g* between them

The average value of the horizontal component of electric field in Fig. 2.5 is given by

$E = \dfrac{V}{g}$, where *g* is the electrode gap, but neither the applied electric field nor the

optical field is uniform. Thus, the electrooptic phase shift $\Delta\varphi$ is reduced by an overlap

factor Γ given by [15]

$$\Gamma = \frac{G}{V} \iint E |E'|^2 \, dA \qquad (2.43)$$

where E' is the normalized optical field distribution and E is the applied electric field.

Equation (2.40) and (2.41) can be written as

$$\Delta\varphi = \left(\frac{\pi l}{\lambda}\right) n_e^3 r_{33} E_z \cdot \Gamma \qquad (2.44)$$

$$\Delta\varphi = \left(\frac{\pi}{\lambda}\right) n_e^3 r_{33} \left(\frac{l}{g}\right) V \cdot \Gamma \qquad (2.45)$$

Optical Intensity Modulator. Phase modulation can be converted to intensity modulation using interference of orthogonal polarization components of the light. This can be achieved by placing linear polarizer with axis oriented at +45° and -45° relative to the optic axis before and after the waveguide, respectively. In this work, optical intensity modulation is accomplished by coupling the light polarized at an angle of +45° relative to the optic axis into the waveguide and placing a linear polarizer (analyzer) oriented at -45° with respect to the optic axis. The linear polarizer at the output converts the phase modulation to intensity modulation. The incident light coupled into the waveguide contains both TE and TM polarization components with the same amplitude. These two waves propagate independently through the waveguide. The electric fields for both TE and TM waves are, respectively,

$$E_x = \frac{E_i}{\sqrt{2}} e^{j(\omega t - \varphi_x)}$$
$$E_z = \frac{E_i}{\sqrt{2}} e^{j(\omega t - \varphi_z)}$$

(2.46)

where the phase shifts are $\varphi_x = k(n_0 + \Delta n_0)l$ and $\varphi_z = k(n_e + \Delta n_e)l$. The electric field transmitted through an analyzer oriented at 90° relative to the incident polarization can be expressed as

$$E_{out} = \frac{E_i}{2} \left(e^{j(\omega t - \varphi_x)} - e^{j(\omega t - \varphi_z)} \right)$$

(2.47)

The output light intensity normalized by the input light intensity is given by [11]

$$\frac{I_0}{I_i} = \sin^2 \left(\frac{\Delta \varphi}{2} \right)$$

(2.48)

where $\Delta\varphi$ is the relative phase retardation experienced by two waves propagating along the crystal given by

$$
\begin{aligned}
\Delta\varphi &= \varphi_x - \varphi_z \\
&= k(n_0 - n_e)l + \frac{1}{2}k\left(n_e^3 r_{33} - n_0^3 r_{13}\right)E_z \cdot l \\
&= k(n_0 - n_e)l + \frac{1}{2}kn_e^3 r_c E_z \cdot l
\end{aligned}
\tag{2.49}
$$

where r_c is the effective electrooptic coefficient defined as

$$
r_c = r_{33} - \left(\frac{n_0}{n_e}\right)^3 r_{13}
\tag{2.50}
$$

Since the first term of equation (2.49) does not represent an electrooptic phase change, the half-wave voltage V_π required for producing a phase change of π radians in the second term of equation (2.49) with the use of $E = \dfrac{V}{g}$ as

$$
V_\pi = \frac{\lambda g}{n_e^3 r_c l}
\tag{2.51}
$$

 Equation (2.48) can be rewritten as

$$
\frac{I_o}{I_i} = \frac{1}{2}\left\{1 - \cos\left(\varphi_0 + \pi\frac{V}{V_\pi}\right)\right\}
\tag{2.52}
$$

where $\varphi_0 = k(n_0 - n_e)l$. Generally, the modulation voltage consists of DC and AC components as $V = V_{dc} + V_m \sin\omega_m t$. Adjusting dc voltage so that $\varphi_0 + \pi\dfrac{V_{dc}}{V_\pi} = \dfrac{\pi}{2}$ with

the use of $\cos\left(\dfrac{\pi}{2} + \theta\right) = -\sin\theta$, the transfer function in equation (2.52) becomes

$$\frac{I_o}{I_i} = \frac{1}{2}\left\{1 + \sin\pi\left(\frac{V_m \sin\omega_m t}{V_\pi}\right)\right\} \tag{2.53}$$

If the value of V_m is very small compared to V_π, equation (2.53) can be rewritten as

$$\frac{I_o}{I_i} = \frac{1}{2}\left\{1 + \pi\frac{V_m \sin\omega_m t}{V_\pi}\right\} \tag{2.54}$$

Equation (2.54) shows that the output transmitted intensity is a linear function of the radio-frequency (rf) modulating voltage $V_m \sin\omega_m t$ as shown in Figure 2.6 [11].
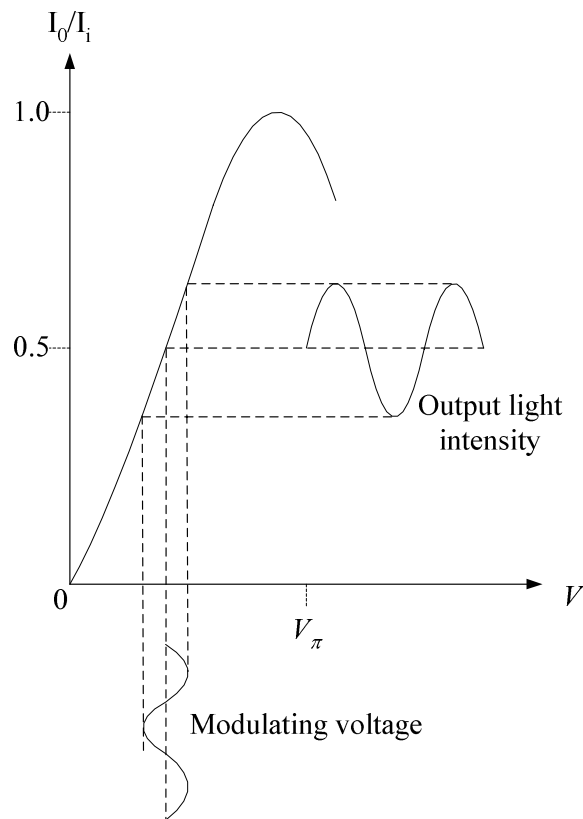
Figure 2.6 Output modulated light intensity versus the modulating voltage

E. Spurious-Free Dynamic Range

Spurious-free dynamic range (SFDR) is a very important parameter to determine the utility of an analog optical transmission link for most applications. It is the usable dynamic range of a signal before spurious harmonics appear to distort the original first-harmonic signal [16]. SFDR is defined as the ratio of the largest to smallest signal that the link can transmit and receive without introducing distortion. Figure 2.7 shows how SFDR is measured for the third order nonlinearity with f being the modulating frequency.
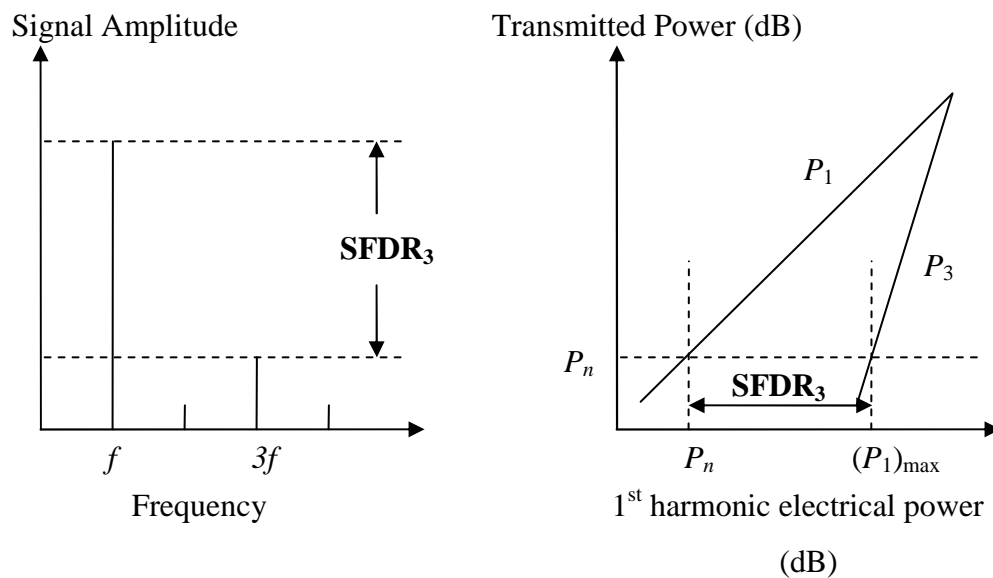
Figure 2.7 Spurious-free dynamic range plot for third-order nonlinearity

The factors which limit the dynamic range in fiber optic links are the system noise, predominantly from laser relative intensity noise; the photodetector shot noise, and the nonlinearity of the modulation process [17]. Biasing an optical modulator at a

quadrature point (half-power point) produces maximum link gain and no even-order distortion [18]. Therefore, quasi-linear operation is achieved over a narrow range of modulating phase shift. The goal of this dissertation research is to extend this quasi-linear range through the use of optical feedback.

The SFDR is generally referenced to a signal power P_n which equals the noise floor of the optical link, as illustrated in Fig. 2.7. In this dissertation research, where the intent is to study the improvement in modulation linearity due optical feedback, an alternative SFDR reference is introduced: 3rd harmonic SFDR with respect to constant optical modulation depth A_0. The purpose is to remove system noise as a factor and provide a measure against which to measure the nonlinearity of the modulator alone.

The ratio of output to input intensity can be written

$$\frac{I_0}{I_i} = \frac{(1 + \sin \phi)}{2} \tag{2.55}$$

with

$$\phi = A \sin \omega_m t \tag{2.56}$$

where, from equation (2.52),

$$A = \frac{\pi V_m}{V_\pi} \tag{2.57}$$

The first two terms in the series expansion of the sine function are $\sin \phi = \phi - \dfrac{\phi^3}{6}$, so that

$$\sin \phi = A \sin \omega_m t - \frac{A^3 \sin^3 \omega_m t}{6} \tag{2.58}$$

But it is easily shown that

$$\sin^3 \omega_m t = \frac{1}{4}\left(3\sin \omega_m t - \sin 3\omega_m t\right) \tag{2.59}$$

Thus, the first harmonic electrical power P_1 is given by

$$P_1 = \left(\frac{A}{2} + \frac{3A^3}{48}\right)^2 I_i^2 R \tag{2.60}$$

with R a load resistance. While the third harmonic power P_3 is

$$P_3 = \left(\frac{A^3}{48}\right)^2 I_i^2 R \tag{2.61}$$

To determine the SFDR at a modulation depth A_0, we set $A = A_0$ in (2.60) and solve for the value of A in (2.61) such that $P_3 = P_1$. If A_0 is $\ll 1$, the second term in (2.60) can be neglected, so

$$A^3 = 24A_0 \tag{2.62}$$

The SFDR for modulation depth A_0 is equal to $(A/A_0)^2$, so that

$$\text{SFDR} = \left(24/A_0^2\right)^{2/3} \tag{2.63}$$

In the experiments described in chapter V section B., the SFDR was measured at a constant modulation depth of 8.36%, or $A_0 = .0836$. From equation (2.63), the theoretical value of SFDR without feedback for an interferometric modulator at this modulation depth is 227.6, or 23.6 dB.

CHAPTER III

DEVICE STRUCTURE AND ANALYSIS

In this chapter, the structure and the principle of operation of an electrooptic intensity modulator with improved linearity is presented. Also, an analysis of this modulator is described.

A. Device Structure and the Principle of Operation

The structure of this electrooptic intensity modulator is shown in Figure 3.1. The modulator consists of a Ti:LiNbO$_3$ straight channel waveguide with electrodes placed on either side of the waveguide. The electrooptic substrate is x-cut, with the light propagating along the y-axis. The channel waveguide is fabricated such that the refractive index of the guiding region is greater than that of the substrate. Light is confined to the vicinity of the waveguide without scattering into the substrate. The waveguide supports a single guided mode for both TE and TM polarizations.

Channel Waveguide

Electrodes

LiNbO$_3$ Substrate
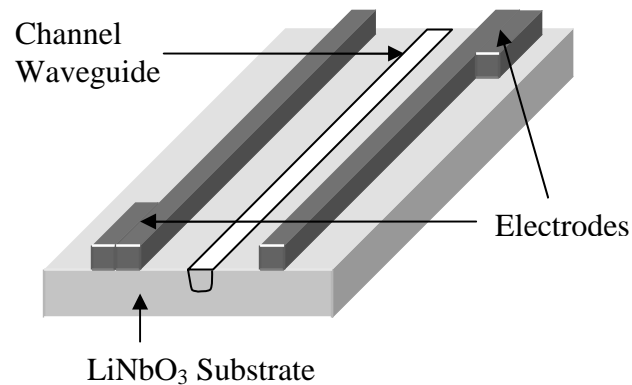
Figure 3.1 Schematic drawing of the device structure

Light is coupled into the waveguide with the polarization vector at an angle of +45° relative to the optic axis; thus, the incident light contains equal amplitudes of both TE and TM polarization components. A modulating voltage applied to the electrodes produces an internal electric field in the waveguide region. The linear electrooptic effect or Pockels effect provides a change in refractive index that leads to a relative phase retardation between the TE and TM modes in the waveguide. Since the electrooptic coefficients which affect the TE and TM polarization modes are different, there is a voltage-dependent shift between them. They are effectively mixed by the output polarizer (analyzer) set at -45° relative to the optic axis to convert the phase modulation to intensity modulation as shown in Figure 3.2.
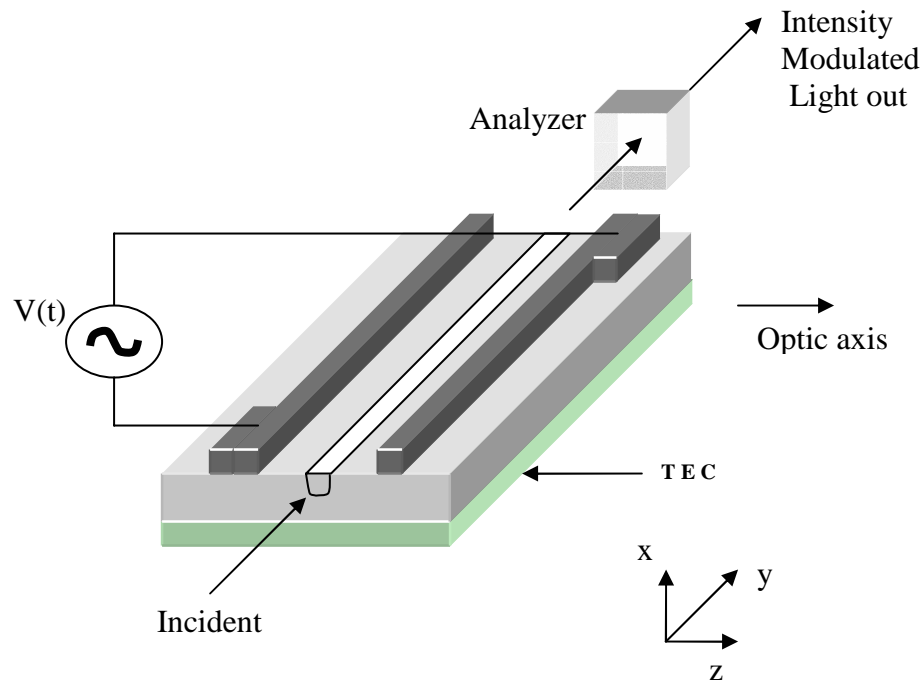
Figure 3.2 An electrooptic intensity modulator in which a linear polarizer
converts the phase modulation into intensity modulation

B. Analysis of Device with Improved Response Linearity Using Optical Feedback

The nonlinearity analysis is the same as for the case of interferometric
modulators such as the Mach-Zehnder modulator (Appendix 17). The nonlinearity in
this modulator results from the nonlinear dependence of the sine function on its
argument. Normally, this analysis neglects the Fabry-Perot effect which results from
reflections at crystal edges. In this work, this optical feedback is taken into account
and used to improve the linearity of the optical modulator. The waveguide axis in this
modulator is oriented perpendicular to the polished edges of the substrate; therefore,
the crystal forms a Fabry-Perot resonator for both TE and TM modes. The effect of

the Fabry-Perot modulation on TE and TM modes is superimposed as a relatively small perturbation on the effect of the relative phase retardation between TE and TM polarizations. This Fabry-Perot effect can be considered to improve the modulation linearity. The model for this analysis is shown in Figure 3.3.
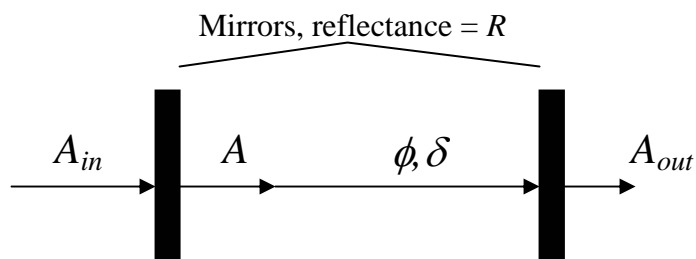
Figure 3.3 Model for analyzing Fabry-Perot effect

The Fabry-Perot interferometer (FPI) or etalon consists of a resonant cavity formed by two parallel mirrors [19]. Let R be the power reflectivity or the reflectance of each of the two mirrors. The reflectance can be calculated by

$$R = \left(\frac{n_1 - n_2}{n_1 + n_2} \right)^2 \tag{3.1}$$

where n_1 and n_2 are refractive index outside and inside the cavity, respectively. The input electric field amplitude A_{in}, and output electric field amplitude A_{out}, are measured immediately before the first and after the second mirror, respectively. The field amplitude in the resonant cavity A, is measured just following the first mirror. On each reflection, the reflected field amplitude is $\sqrt{R}$ times the incident field amplitude.

Mirrors, reflectance $= R$
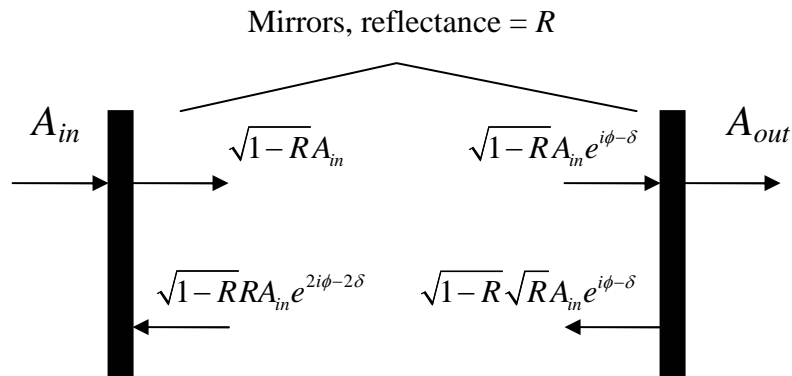
Figure 3.4 How the light reflects inside the cavity of Fabry-Perot resonator

Electric field strength of successive reflections is illustrated in Figure 3.4. Initially, it is assumed that no field is present. Then, the input electric field with amplitude A_{in} is applied and produces a field in the cavity of

$$A = \sqrt{1-R}A_{in} \qquad (3.2)$$

The light experiences a phase shift of ϕ radian and amplitude attenuation of $e^{-\delta}$ in propagating from one mirror to the other, and a $\pi/2$ phase shift at each reflection. The light first arrives at the second mirror with the field amplitude $\sqrt{1-R}A_{in}e^{i\phi-\delta}$ and a portion $\sqrt{1-R}\sqrt{R}A_{in}e^{i\phi-\delta}$ is reflected back to the first mirror. This portion arrives at the first mirror and is reflected back toward the second where the field amplitude of light that has made one round trip can be expressed as $\sqrt{1-R}RA_{in}e^{2i\phi-2\delta}$. The amplitude of the light just entering the cavity through the first mirror adds to that which has made one round trip to give

$$A = \sqrt{1-R}A_{in} - \sqrt{1-R}RA_{in}e^{2i\phi-2\delta} \tag{3.3}$$

After N round trip, A can be expressed as

$$A = \sqrt{1-R}A_{in}\sum_{n=0}^{N}a^{n} \tag{3.4}$$

where

$$a = -R \cdot e^{2i\phi-2\delta} \tag{3.5}$$

It is assumed that a steady state condition has been reached by $N \to \infty$ and $|a| < 1$,

then

$$\sum_{n=0}^{N}a^{n} = \frac{1}{1-a} \tag{3.6}$$

Therefore, the steady state value of A is

$$A = \frac{\sqrt{1-R}}{1-a}A_{in} \tag{3.7}$$

This light following the first mirror, whose amplitude is A, travels through both the cavity and second mirror before leaving the second mirror with a field amplitude, A_{out}, that can be written as

$$A_{out} = A_{in}\frac{(1-R)e^{i\phi-\delta}}{1-a} \tag{3.8}$$

This A_{out} in equation (3.8) can be expressed in terms of real and imaginary parts as

$$A_{out} = A_{in}\frac{(1-R)(1-a^{*})e^{i\phi-\delta}}{(1-a)(1-a^{*})} \tag{3.9}$$

Substituting equation (3.5) into equation (3.8) yields,

$$A_{out} = A_{in} \frac{(1-R)\cos\phi(e^{-\delta} + Re^{-3\delta}) + i(1-R)\sin\phi(e^{-\delta} - Re^{-3\delta})}{1 + R^2 e^{-4\delta} + 2Re^{-2\delta}\cos 2\phi} \tag{3.10}$$

The complex amplitude A_{out} for TE and TM modes is different because of the different refractive indices and attenuation of the LiNbO$_3$ waveguide modes in each case. Let $\alpha = z$ correspond to TE polarization and $\alpha = x$ correspond to TM polarization. The values R_α, δ_α, and ϕ_α, with the previous convention of α, are used to determine the amplitude $A_{\alpha out}$ for each polarization. For example, using $n_z = 2.137$ and $n_x = 2.216$, corresponding respectively to extraordinary and ordinary refractive indices for LiNbO$_3$ at 1.55 µm, $R_z = 0.131$ and $R_x = 0.143$ at air interfaces. The phase shifts for both polarizations can be written as the function of modulation voltage, V, as

$$\phi_\alpha = \phi_{\alpha 0} + K_\alpha V \tag{3.11}$$

where K_α is an electrooptic coefficient. The desired values of input phase shift ϕ_{z0} and ϕ_{x0} can be adjusted by changing the temperature of the substrate to affect the modulator response linearity. There are multiple temperatures which can yield the same value of ϕ_{x0} or ϕ_{z0}, because of the fact that equivalent of phase shift values are separated by 2π.

If the electric field amplitude of the incident light is normalized to 1 at an angle of θ_{in} relative to the optic axis (z-axis), then

$$A_{\alpha in} = \begin{cases} \sin\theta_{in} & ;\alpha = x \\ \cos\theta_{in} & ;\alpha = z \end{cases} \tag{3.12}$$

The output power for the modulator results from the interference of orthogonally polarized waves and is the fraction of the input optical power transmitted through an analyzer. It can be written as

$$P_{out} = \left| A_{xout} \sin \theta_{out} + A_{zout} \cos \theta_{out} \right|^2 \tag{3.13}$$

with the angle of the transmission axis of an analyzer, θ_{out}, relative of an optic axis. Using equation (3.10)-(3.13), it is possible to calculate P_{out} as a function of V. Output optical power $(P_{out})_k$ can be calculated for M discrete values of V with a small increment ΔV given by

$$V_k = \left(k - \frac{M-1}{2} \right) \Delta V \quad ; k = 0,1,2...,M-1 \tag{3.14}$$

The value of signal photocurrent, I_s, is considered to observe the nonlinearity. This photocurrent is proportional to P_{out} as $I_s = \rho P$ where ρ is the sensitivity of the photo detector. Therefore, each value of $(I_s)_k$ is proportional to each one of $(P_{out})_k$ for $k = 0$, 1, 2,…, M-1 as

$$\left(I_s \right)_k = I_0 \sum_{m=0}^{M-1} c_m \left(V_k \right)^m \quad ; k = 0,1,2,...,M-1 \tag{3.15}$$

where $c_0 I_0$ is the photocurrent without the modulation and M-1 is the degree of the polynomial fit. To analyze the nonlinearity, the M real values of coefficients c_m are obtained by using numerical method for solving M simultaneous equations of equation (3.15). Then, these values of c_m's are used to determine the modulator's spurious-free dynamic range for each harmonic. Normally, a modulating voltage is a sinusoidal function with amplitude, A, and can be expressed by

$$V = A\cos(\omega t) \tag{3.16}$$

Equation (3.16) can be rewritten in exponential form, using Euler's equation, as

$$V = A\left(\frac{e^{i\omega t} + e^{-i\omega t}}{2}\right) \tag{3.17}$$

Using equation (3.16), I_s can be written as

$$I_s = I_0\left\{c_0 + c_1 A\cos(\omega t) + c_2 A^2 \cos^2(\omega t) + ...\right\} \tag{3.18}$$

Assume that $c_2 \ll c_0$, equation (3.18) yields

$$I_s = I_0\left\{c_0 + c_1 A\cos(\omega t) + c_2 \frac{A^2 \cos(2\omega t)}{2} + ...\right\} \tag{3.19}$$

The electrical signal power at the first two harmonic P_{s1} and P_{s2} are given by

$$P_{s1} = \frac{RI_0^2 c_1^2 A^2}{2} \tag{3.20}$$

$$P_{s2} = \frac{RI_0^2 c_2^2 A^4}{8} \tag{3.21}$$

with R is the load resistance. While the noise power of photodetector is dominated by a shot noise which is given by

$$P_n = 2eRc_0 I_0 B \tag{3.22}$$

Following from equation (3.21) and equation (3.22), the value of A^2 that makes the second harmonic power equal the noise power is

$$A^2 = \frac{4}{c_2}\left(\frac{ec_0 B}{I_0}\right)^{\frac{1}{2}} \tag{3.23}$$

The SFDR_n represents the range of electrical power which can be generated in the receiver by the value at which the n-harmonic electrical power equals the noise power. It can be defined as the ratio of P_{sn} to P_n. Therefore, SFDR_2 is the ratio of P_{s2} to P_n for the value of A in equation (3.23), which is given by

$$\text{SFDR}_2 = \frac{c_1^2}{c_2}\left(\frac{I_0}{eC_0B}\right)^{\frac{1}{2}} \tag{3.24}$$

The same approach is used to determine the third-order nonlinearity starting with the third-order term of equation (3.18) as

$$I_{s3} = \frac{I_0 c_3 A^3 \cos(3\omega t)}{32} \tag{3.25}$$

Thus, the electrical signal power at the third harmonic, P_{s3}, is expressed as

$$P_{s3} = \frac{R I_0^2 c_3^2 A^6}{32} \tag{3.26}$$

Thus, SFDR_3 can be given by

$$\text{SFDR}_3 = \frac{c_1^2}{c_3^{2/3}}\left(\frac{I_0}{ec_0B}\right)^{\frac{2}{3}} \tag{3.27}$$

Therefore, the general formula for SFDR_n can be written as

$$\text{SFDR}_n = \frac{Q_n c_1^2}{c_n^{2/j}}\left(\frac{I_0}{ec_0B}\right)^{1-\frac{1}{n}} \tag{3.28}$$

where Q_n is a constant value for each harmonic.

The analysis so far has dealt with harmonics ω_j of the fundamental radian frequency ω_1. In case of modulating signals with 2 frequencies of ω_a and ω_b, the

SFDR still yields the same general formula of equation (3.28) except the value of Q_n is different. Table 3.1 shows the values of coefficients Q_n for harmonic analysis and Q'_n for intermodulation analysis. It can be clearly seen from the value of Q'_n's that the *SFDR* becomes lower when intermodulation products are considered.

Table 3.1 The values of the coefficients Q_n (harmonic) and Q'_n (intermodulation)

	n				
	2	3	4	5	6
Q_n	1.0	1.0	0.5	0.525	0.405
Q'_n	0.5	0.481	0.204	0.209	0.149

From above analysis, these parameters R_x, R_z, δ_x, δ_z, $\phi_{x0,}$ and ϕ_{z0} are needed to be attuned to achieve a high SFDR. The reflectance values of R_x and R_z can be adjusted by applying some index-matching fluid or thin film coatings to one or both ends of the substrate. The value of δ_x and δ_z can be adjusted by changing the length of the substrate. The longer the substrate is the greater the value of the amplitude loss coefficient δ is. The phase shift $\phi_{x0,}$ and ϕ_{z0} can be tuned by changing the temperature of the substrate.

CHAPTER IV

DEVICE FABRICATION

The process for fabrication of an electrooptic light modulator is presented in this chapter. The process consists of two main procedures: Ti:LiNbO$_3$ straight channel waveguide fabrication, and metal-electrode fabrication. Fabrication parameters are shown in this chapter, and a step-by-step outline of the process is given in Appendix 1.

A. Ti:LiNbO$_3$ Straight Channel Waveguide

There are several methods to fabricate optical channel waveguides. The conventional thermal titanium in-diffusion technique is used in this work. The details of the channel waveguide fabrication process are described below.

First, a 72-mm. diameter, 1-mm. thick *x*-cut LiNbO$_3$ crystal wafer supplied by Crystal Technology Inc. (Palo Alto, CA) was cut using the dicing machine (Appendix 2) into several small samples with dimensions of 9 mm. along the *z*-axis and 25.4 mm. along *y*-axis for making straight channel waveguides with light propagation in the *y*-direction. These small substrates were cleaned with liquid solvents (Appendix 3). A Ti film of thickness in the range 1,040 Å to 1,100 Å was deposited onto the substrates with a DC sputtering process (Appendix 4). A positive photolithography process (Appendix 5) was applied to pattern the desired straight channel waveguides on top of the Ti film. After the photoresist was developed, the substrates were inspected under a microscope to ensure the quality of the channel waveguide patterns. A very thin layer

of photoresist left from the previous process on each substrate was taken off chemically using Plano descum. The substrates were cleaned in a barrel asher with oxygen plasma at 135°C for 3 minutes (Appendix 6). This oxygen plasma also hardens the patterned photoresist to endure in the reactive ion etching (RIE) process (Appendix 7). Unwanted portions of Ti on the substrates were removed by RIE. Typically, the RIE process is anisotropic, and is preferred over wet etching because it preserves the desired Ti channel waveguide width, and gives good sidewall smoothness. However, to prevent the substrate surface from being over etched, it is critical to etch the Ti film to such an extent that a thin layer of Ti is left on after the RIE process [20]. The remaining Ti film was later completely moved by an acid wet etch with diluted hydrofluoric (HF) acid (Appendix 8). However, it is very difficult to control the wet etching process to avoid overetching. Oxidation of Ti in air leaves a very thin layer of titanium oxide on the surface of the substrate. This titanium oxide layer reacts very slowly with the HF acid, whereas pure Ti is removed rapidly. When the oxide layer is etched, the pure Ti is removed rapidly. This probably leads to waveguide undercutting which narrows the waveguide width and produces rough edges. Therefore, a proper acid solution and wet etching time is very important to obtain a good etching result. An acid solution of HF:DI Water with the ratio of 1:20 and an etching time of 8 to 10 seconds was proven to work well.

After wet etching, the substrate was put in a heated photoresist stripper, Clariant AZ300T, at a temperature of 90°C for 20 minutes to remove the remaining photoresist from the substrate surface. Then, solvents such as acetone and methanol

were used to clean the substrate prior to the measurement of both the channel waveguide's pattern width and the thickness of the Ti film. The width of the Ti straight channel waveguide pattern was inspected under a high-magnification microscope. The thickness of the Ti film was measured with a Dektak[3] Surface Profile Measuring System.

Then, the substrate was put into a diffusion furnace (Appendix 9) under a wet oxygen ambient to obtain a high index optical waveguide at a temperature in the range 1,025ºC to 1,050ºC for 10 to 13 hours, depending on the thickness of the Ti film. The wet air ambient treatment was used to reduce Li_2O out-diffusion, which can cause unwanted planar guiding for the extraordinary polarization, the TE mode on this work, and lead to considerable increase in the propagation loss [21]. Several parameters such as the thickness of in-diffused Ti on the substrate, the diffusion time, and temperature in the diffusion furnace were optimized to achieve good quality channel waveguides. A good quality waveguide in this work exhibits single mode characteristics with low propagation loss and strong confinement of light for both TE and TM modes. The temperature of the diffusion furnace, T, is more critical than the diffusion time, t, as indicated by the following equation [22].

$$d = 2\sqrt{Dt} \tag{4.1}$$

with d the diffusion depth and

$$D = D_0 e^{-T_0/T} \tag{4.2}$$

where D_0 is the bulk diffusivity and T_0 is the activation temperature. Both D_0 and T_0 depend on the LiNbO$_3$ composition. For 48.6 mole % of Li$_2$O in LiNbO$_3$, $T_0 = 2.5 \times 10^4$ K and $D_0 = 2.5 \times 10^{-4}$ cm^2/s [22].

After the diffusion process, both ends of the substrate were polished (Appendix 10), so that the light can be coupled into the waveguide. To achieve a good fiber-to-waveguide coupling, a good optical finish and 90º edge are required at both input and output optical faces [23].

B. Electrooptic Light Modulator

The electrode patterns were produced on the substrate from the previous process to obtain an electrooptic light modulator. Electrode patterns as shown in Figure 4.1 were delineated in photoresist by an image reversal photolithography process (Appendix 11).
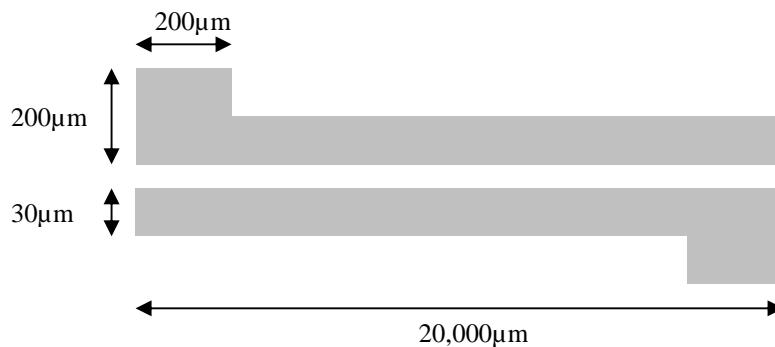
Figure 4.1 Schematic drawing of electrodes

The baking and exposing time are very critical to have good image reversal pattern on the substrate. The pattern was carefully inspected under microscope prior to the metal deposition to ensure that the desired areas are properly open for deposited metals in later stage of the process. The thicknesses 500 Å of Cr, 1,500 Å of Al, and 1,000 Å of Au were deposited on the substrates using electron beam (E-beam) evaporation (Appendix 12). The Cr layer, the first electrode layer, was used to improve the adhesion of the metal to the surface of the substrate. The Au layer was used because of its high electrical conductivity. Finally, the lift-off process (Appendix 13) was used to remove the metal deposited on the photoresist, leaving the desired electrode pattern. Then, the substrate was thoroughly cleaned prior to the optical tests.

CHAPTER V

OPTICAL TESTING AND RESULTS

In this chapter, the performance results of channel waveguides, including insertion loss and mode profile scans, are shown. The results of tests on modulator SFDR and linearity are also presented.

A. Channel Waveguides

To obtain good optical modulator performance, a high quality channel waveguide is required. This waveguide should be single mode with low propagation loss and strong confinement of light for both TE and TM polarization modes. The output optical power for TE and TM polarizations is optimized by controlling parameters such as the thickness of in-diffused Ti on the substrate, the time, and temperature inside the diffusion furnace. The waveguide insertion loss is the total amount of optical intensity lost through a device. This consists of a mode mismatch loss, Fresnel reflection loss, and propagation loss. Insertion loss can be written in dB as

$$\text{Insertion Loss } (dB) = -10 \log \frac{P_{out}}{P_{in}} \tag{5.1}$$

with P_{in} and P_{out} an input and output light intensity, respectively. The mode mismatch loss results from the difference of the mode profile between the fiber and the waveguide. It can be calculated using the measured near-field mode profile. The

coupling efficiency can be determined by calculating the overlap between the fiber and waveguide modes. The power coupling coefficient can be written as [24]

$$\kappa = 0.93 \left[\frac{4}{\left(w_x/a + a/w_x\right)\left(w_y/a + a/w_y\right)} \right]$$

(5.2)

where a is the fiber mode intensity diameter which is 10.5 µm for SMF-28 single mode fiber at 1.55 µm wavelength [25], w_x, w_y are defined as the waveguide mode width and depth at $1/e$ of maximum intensities, respectively, and the constant of 0.93 accounts for the mismatch between the symmetric fiber and the diffused channel waveguide mode assuming identical $1/e$ dimensions for the two. Thus, the mode mismatch can be expressed as

$$\text{Mode mismatch loss (dB)} = -10\log\kappa$$

(5.3)

Fresnel loss is caused by the reflection of light at the two end of the crystal. It is given by 1-R where R is the reflectance. At normal incidence, the reflectance can be calculated from

$$R = \left(\frac{1 - n_{0,e}}{1 + n_{0,e}}\right)^2$$

(5.4)

with n_0 and n_e the ordinary and extraordinary reflective indices of the crystal, respectively. Thus, the Fresnel reflection loss can be expressed by

$$\text{Fresnel Loss (dB)} = -20\log\left(1 - R\right)$$

(5.5)

This Fresnel reflection loss can be reduced by using either index-matching fluid or antireflection coatings on the crystal edges [26]. Propagation loss is caused by

a combination of optical absorption and optical scattering in the channel waveguide. Once the insertion loss, Fresnel reflection loss, and mode mismatch loss are known, the propagation loss can be found in the unit of dB/cm by

$$\text{Propagation Loss} = \frac{\text{Insertion loss} - \left(\text{Mode Mismatch loss} + \text{Fresnel loss}\right)}{L} \quad (5.6)$$

with all other losses in unit of dB, and L in units of cm.
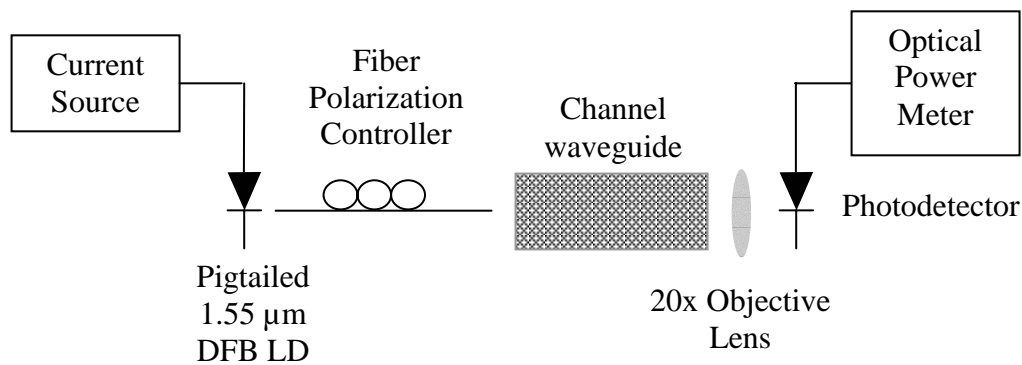
Figure 5.1 Test setup for insertion loss measurement

The optical test setup to measure insertion loss is shown in Figure 5.1. A pigtailed 1.55 µm distributed feedback (DFB) laser diode (Alcatel, Module: 1915-LMI) driven by a current source laser diode controller (ILX Lightwave, Model: LDC-3742B) at 36.76 mA and 20ºC temperature setting supplied 1 mW of optical power at λ = 1,558.2 nm. The laser diode was spliced to a single mode fiber (Corning SMF-28$^{\text{TM}}$), and the light passed through a fiber polarization controller (Thorlabs Inc.,

Model: FDC010) used to control the polarization of the light before it is launched into the channel waveguide. The light was butt coupled to a waveguide through a polished edge of the substrate. The output 20x objective lens was used to collect the output light coming out of the waveguide and focus it onto a InGaAs p-i-n photodetector (OSI Fibercomm, Model: FCI-In-3000-10), which was connected to an optical power meter (Newport, Model: 1825-C).

Many samples have been fabricated with different Ti-thickness, waveguide widths, and diffusion conditions. Sample # 18, with Ti-thickness of 1,090 Å and 10 hours of diffusion at 1,035ºC, was tested using the above mentioned setup. The sample was 22.5 mm. long. The results of insertion loss measurements are shown in Table 5.1.

Table 5.1 Channel waveguide insertion loss for sample # 18 for both TE and TM polarizations with different channel widths

Insertion Loss W/G Width (μm)	TE mode (dB)	TM mode (dB)
7	3.01	3.16
8	2.61	2.72
9	2.56	2.72

The spatial mode profile (dependence of optical power on position) is measured using the setup illustrated in Figure 5.2 to determine waveguide quality. At the input side, the setup is the same as the insertion loss measurement setup. On the

output side, a vibrating mirror and a 100 µm wide slit was used to deflect the output

light onto the Ge Photodetector (Newport, Model: 818-IR). The output port of an

optical power meter was connected to a BNC mount accessory (National Instrument,

Model: BNC-2090) which was connected to a personal computer via a Data

Acquisition (DAQ) board (National Instruments, AT-MIO-16E-1) to display and

acquire the data using a LabVIEW™ program. A vibrating mirror was driven by a

circuit that scans the beam horizontally or vertically to obtain a near field intensity

distribution of the light. The slit put in front of the detector was oriented vertically for

the horizontal scans (transverse lateral), and was oriented horizontally for the vertical

scans (transverse depth).
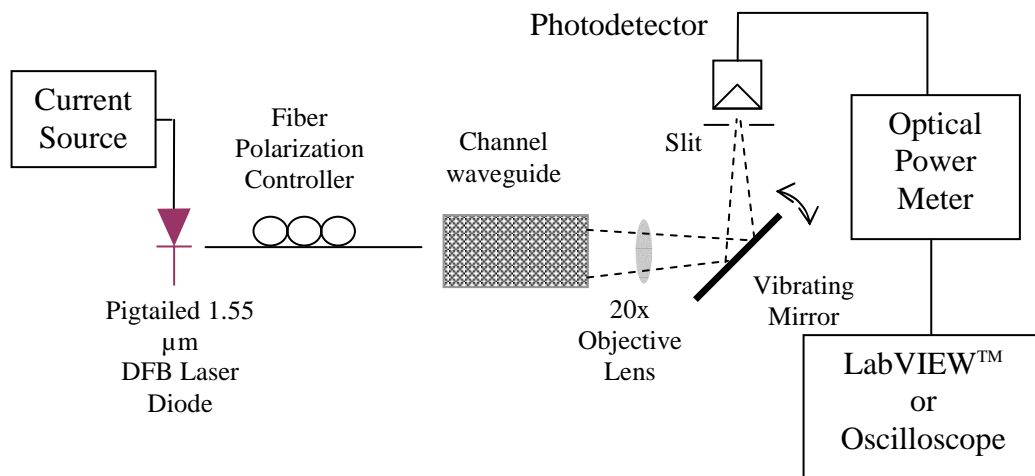
Figure 5.2 Mode profile measurement setup

The results of those scans provide mode profiles corresponding to transverse lateral and transverse depth near field distributions, respectively. The full width at half maximum (FWHM) was measured to evaluate the mode confinement of channel waveguides. Mode profiles for a 7 µm wide channel waveguide on sample # 18 are shown in Figure 5.3.
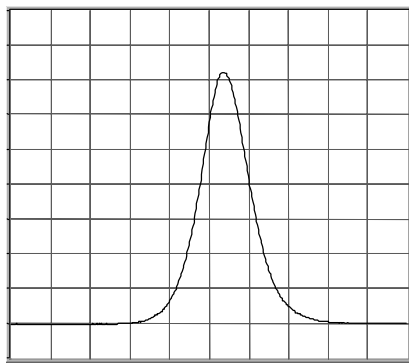
(a) TE Horizontal Scan
(b) TE Vertical Scan
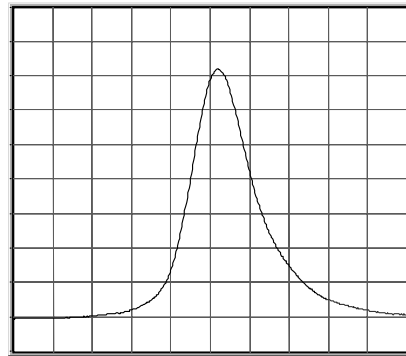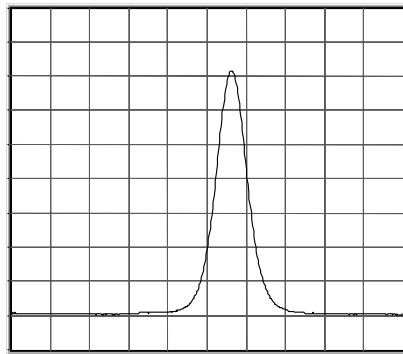
(c) TM Horizontal Scan
(d) TM Vertical Scan

Vertical scale for all scans is 100 mv/div and horizontal scale for TE is 4.69 µm/div and TM is 8.12 µm/div

Figure 5.3 Mode profile of a 7 µm wide channel waveguide on sample # 18

The mode profiles clearly show that the waveguide supports both TE and TM polarization modes. There is only one peak in each scan showing that only the fundamental mode is supported by this channel waveguide. The horizontal scans show that the mode profiles are symmetric and have a nearly Gaussian intensity distribution. The vertical scans show that the mode profiles are asymmetric as expected since the vertical refractive index distribution is highly asymmetric. The measured mode profile dimensions for a 7 µm wide channel waveguide on sample # 18 are given in Table 5.2.
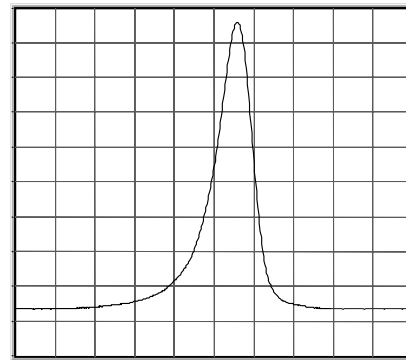
Table 5.2 Measured mode profile dimensions for a 7 µm wide channel waveguide on

sample # 18

Mode Scan	TE	TM
Horizontal FWHM (µm)	6.56	7.93
Vertical FWHM (µm)	7.46	7.98

B. Modulation Test

The modulation performance is tested using the setup in Figure 5.4. The input DFB laser (same models for the laser and controller as for the insertion loss measurement setup) was spliced to a Corning SMF-28^{TM} fiber, which is connected to the 90:10 directional coupler. The 10% output of this directional coupler was used to monitor the stability of the laser intensity. Most of the light went through the 90% part of the directional coupler.
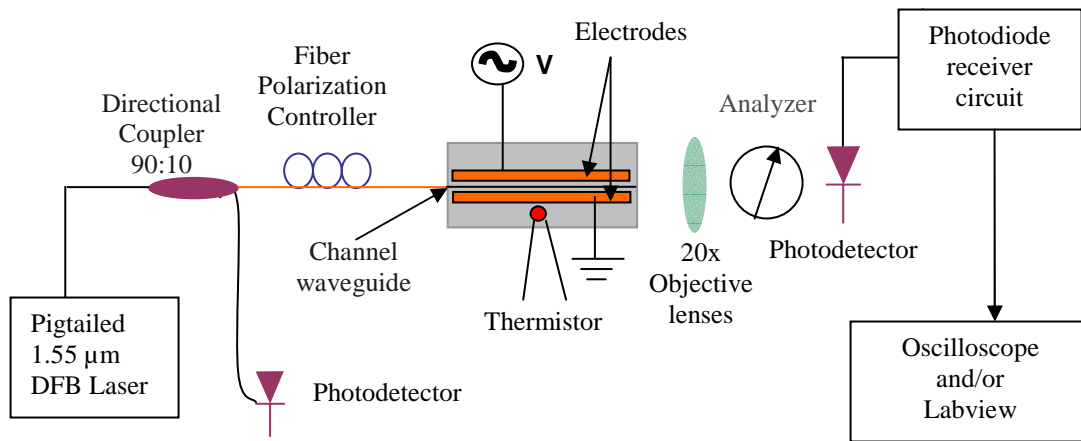
Figure 5.4 Modulation test setup

Light from the 90% leg of the directional coupler was coupled into a polarization controller (Thorlabs Inc., Model: FDC010) oriented at 45º relative to the optic axis. Equal amounts of TE and TM light were coupled into the channel waveguide. A function generator (Hewlett Packard, Model: HP 3325B) and a power supply amplifier (Hewlett Packard, Model: HP 6824A) were used to apply a modulating voltage to the electrodes. The output light from the channel waveguide was collected using a 20x objective lens, before being focused into an analyzer (Newport, Model: GT-25A10) oriented at -45º relative to an optic axis, to produce intensity modulated output light. The intensity modulated light was focused onto an InGaAs p-i-n photodetector (OSI Fibercomm, Model: FCI-In-3000-10) and its receiving circuit, which was connected to an oscilloscope or LabVIEW™ board to acquire and display data. The modulation performance of a device # 18 with a single

mode waveguide width of 7 µm, an electrode interaction length of 20 mm, and a gap

between electrodes of 21µm is shown in Figure 5.5.
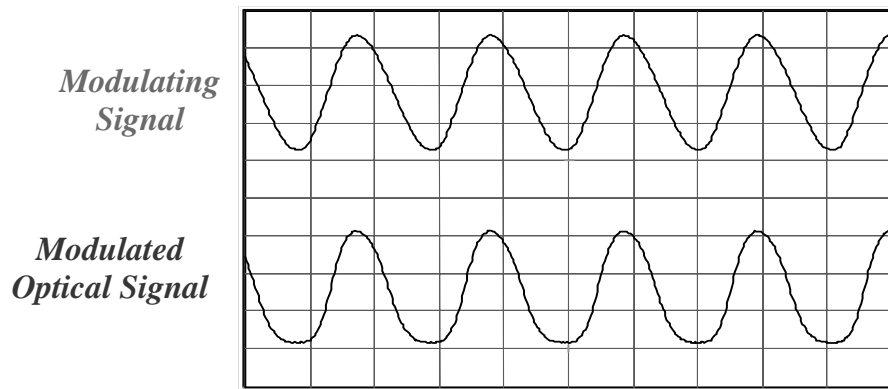
Figure 5.5 The modulation performance of sample # 18. The top waveform is an

applied electrical signal, and the bottom one is a modulated optical output signal

Table 5.3 Length and diffusion parameters of device samples

Sample	# 17	# 18	# 21
Sample Length (mm)	22.5	22.5	23.9
Ti-Thickness (Å)	1,085	1,090	1,040
Diffusion Temperature (°C)	1,035	1,035	1,025
Diffusion Time (hours)	13	10	10

Sample # 17 and sample # 21 were tested on their 7 µm wide single mode

channel waveguides in the same manner as the previous sample (# 18) to observe their

modulation performance. The properties of samples are shown on Table 5.3. Table 5.4 summarizes the modulation performance of those mentioned samples.

Table 5.4 Performance of intensity modulation on various samples

Sample	# 17	# 18	# 21
Modulation Depth (%)	98.5	97.2	96.4
V_π (Volts)	13.8	14.1	14.0

The birefringence of the waveguide; i.e., the phase shift experienced between TE and TM polarization modes, can be tuned by varying the substrate temperature. By slowly increasing the substrate temperature and monitoring the optical output power, temperatures, and temperature ranges in which the modulator linearity is best can be identified. A thermoelectric cooler (Melcor, Model: CP 0.8-71-06L) was placed under the crystal to control the substrate temperature as shown in Figure 5.6.

Thermo-electric Cooler
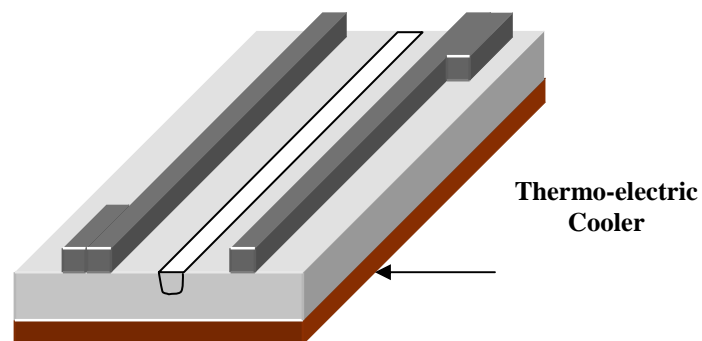
Figure 5.6 A thermo-electric cooler arrangement for adjusting the device temperature

By using the same setup as the intensity modulation test (Figure 5.4) without applying a modulating voltage, the transmitted optical output power out of the waveguide was thermal-modulated by slowly increasing the temperature of the substrate. A thermistor was placed onto the crystal surface to read the temperature. The temperature and optical output power were monitored and recorded with the LabVIEW™ data acquisition system. The dependence of output power on temperature is illustrated in Figure 5.7. Temperatures in the middle of the linear regions, for example, points 1 and 2 in Figure 5.7, were candidate operating temperatures for achieving a high degree of linearity in the electrooptic modulator.
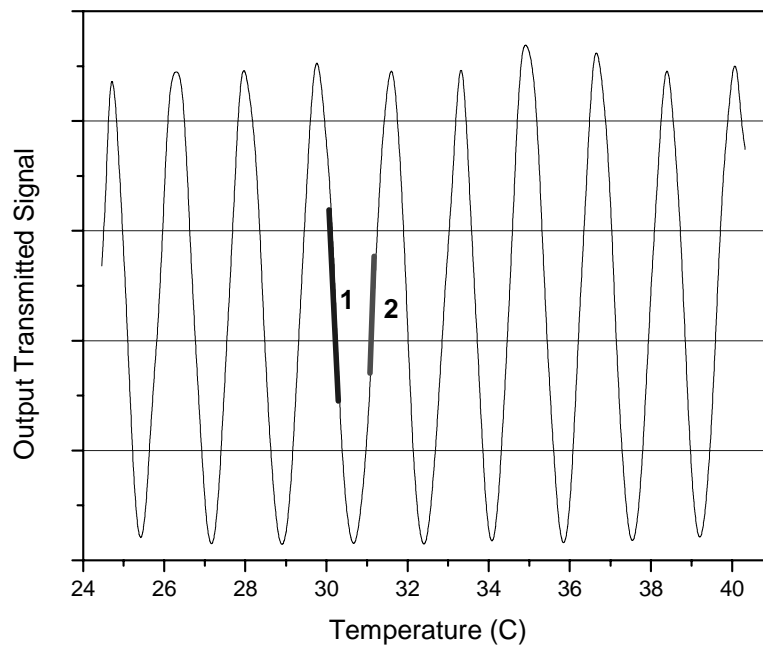
Figure 5.7 Measured optical output intensity on a 7 μm waveguide of sample # 18 plotted while slowly heating the substrate

Three different Fresnel reflectance conditions were used to investigate the effect of feedback on modulation linearity. First, the modulator crystal edges interface with air. Then, reflective index-matching fluid ($n \approx 1.45$) was placed on an input side of the crystal to match the index of the fiber. The last case was that reflective index-matching fluid was applied on both crystal ends using SMF-28[TM] fiber to couple an output light as shown in Figure 5.8.
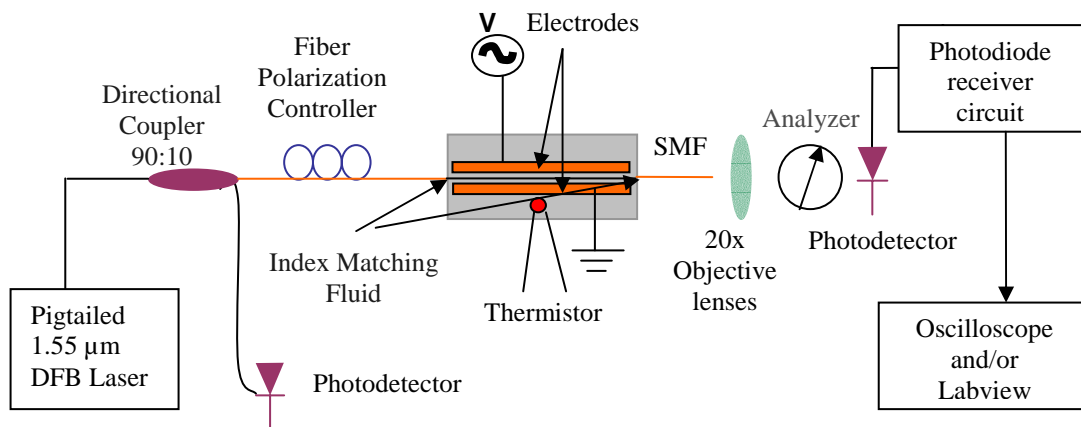
Figure 5.8 Linearity test setup with index-matching fluid applied to both crystal edges, using a single mode fiber to couple light out of the substrate

A sinusoidal voltage signal, of frequency f_m and amplitude V_m is applied to the electrodes, and the detected optical output signal serves as the input to a spectrum analyzer (LabVIEW[TM] software). The electrical power is measured as a function of V_m for the first and higher harmonics of f_m. The linearity is determined by the degree to which the higher harmonics are present as V_m increases. The three different substrate

edge conditions were used to give different levels of feedback. In each case, the modulating voltage was slowly increased while the spectrum of the first and higher harmonics of the optical signal were carefully monitored and recorded. The 7 μm wide channel waveguide with electrode gap of on sample # 21, with an electrode pattern with interaction length of 20 mm and a gap between electrodes of 21μm, was modulated with f_m = 5 kHz at room temperature with three different feedback levels as indicated in Table 5.5. The results are illustrated in Figure 5.9.
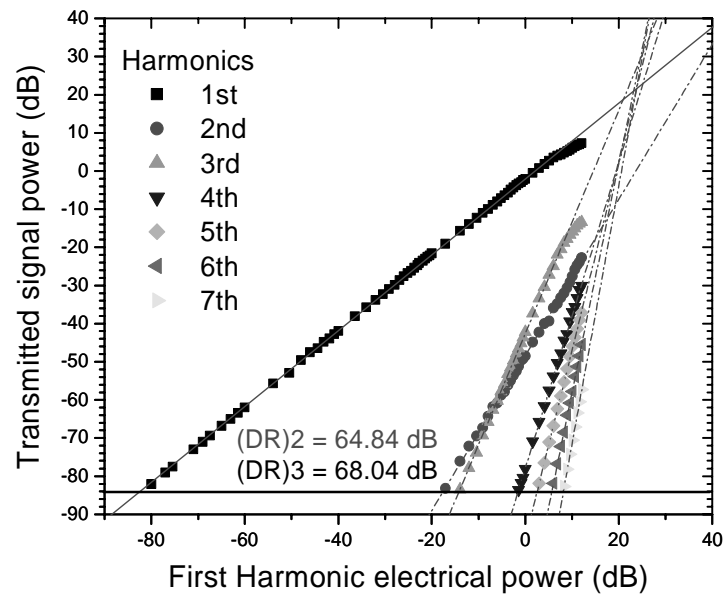
(a) Index-matching fluid was applied at both edges of a substrate

Figure 5.9 Plot of first and higher harmonics for a 7 μm wide waveguide modulator on sample # 21 at T = 23.31°C (room temperature)
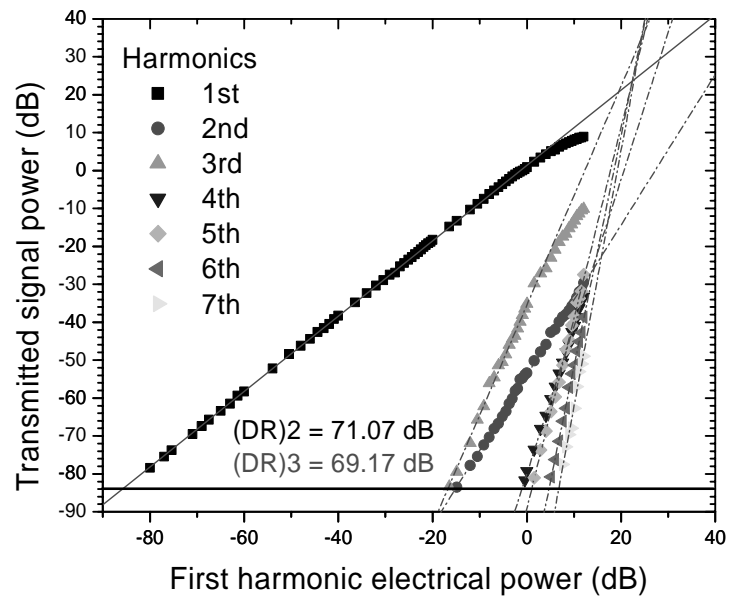
(b) Both edges of a substrate were interfacing air
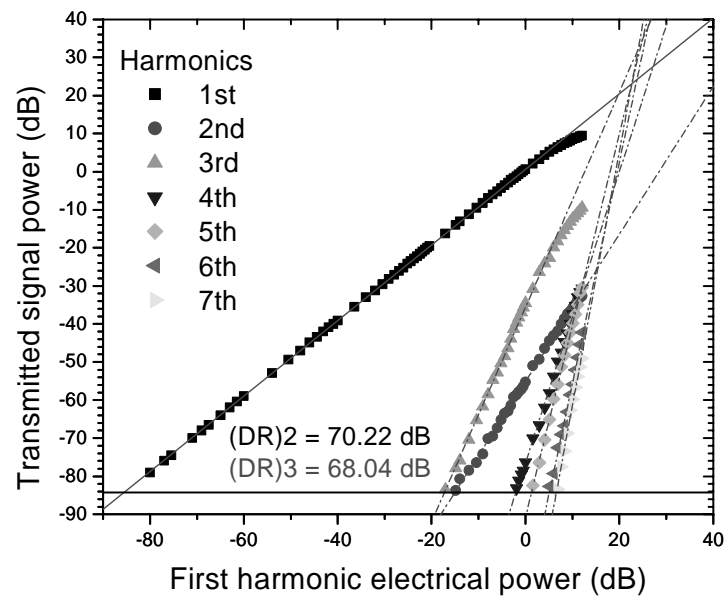
(c) Index-matching fluid was applied at the input edge of a substrate only

Figure 5.9 (continued)

Table 5.5 Reflectance values for various substrate end conditions

Substrate End Conditions	R_{TE}	R_{TM}
Interfacing Air at both ends	0.131	0.143
Index-matching placed at both ends	0.0367	0.0437
Index-matching placed at input end only	0.0680	0.0757

From Figure 5.9, with index-matching fluid applied to both input and output edges of the substrate (case a), the second harmonic limits the SFDR to 64.84 dB. In case b, in which both edges of the substrate interface with air, the third harmonic limits the SFDR to 69.17 dB, while with index-matching fluid put at the substrate input end only (case c), the linearity was limited by the third harmonic to 68.04 dB. It is clearly seen that with different feedback conditions, the SFDR was limited by different harmonics and yields different SFDR values.
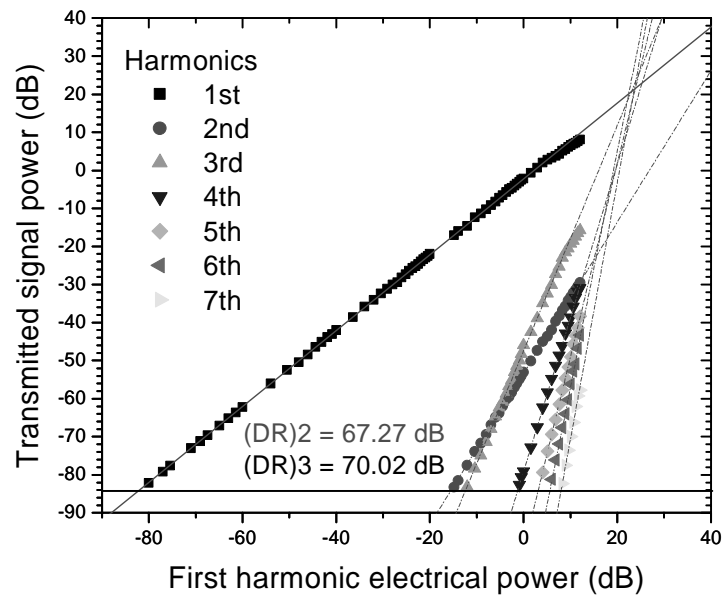
(a) Index-matching fluid was applied at both edges of a substrate
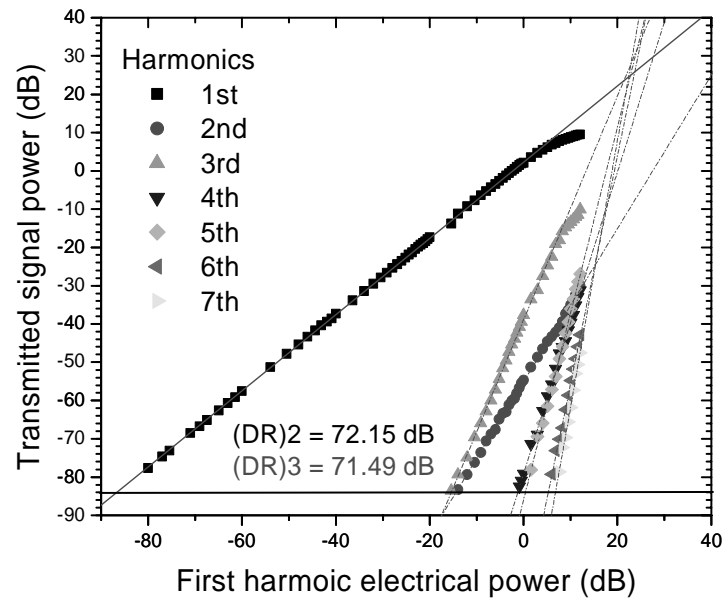
(b) Both edges of a substrate were interfacing air

Figure 5.10 Plot of first and higher harmonics for a 7 μm wide waveguide modulator

on sample # 21 at T = 37.67°C
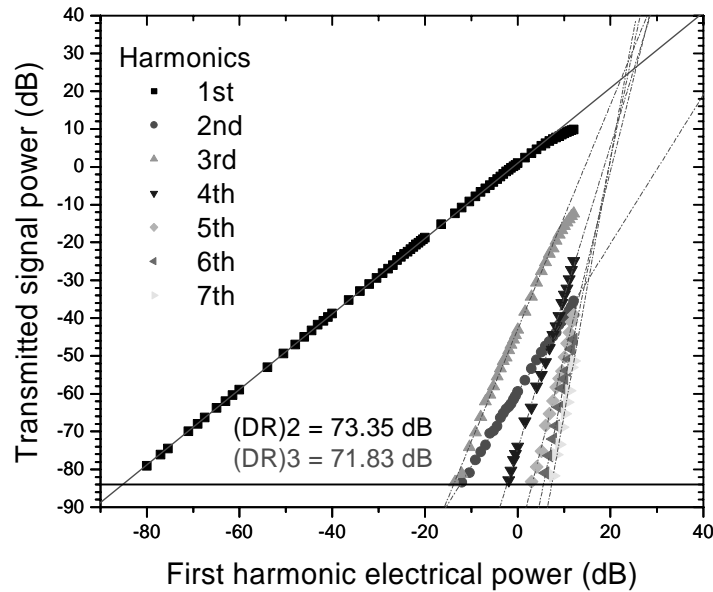
(c) Index-matching fluid was applied at the input edge of a substrate only

Figure 5.10 (continued)

However, the SFDR could also be improved by adjusting the phase shift with changing the temperature of the substrate as mentioned in Chapter 3. Therefore, the data in Figure 5.7 for the 7 μm wide waveguide on sample # 21 was used in selecting substrate temperatures. The modulation results with a sample temperature of 37.67°C are shown in Figure 5.10. With index-matching liquid applied to both crystal ends, the SFDR limited to 67.27 dB by second-order nonlinearity. With no index-matching fluid, and with fluid only at the input end, the SFDR was limited by the third harmonic to 71.49 and 71.83, respectively. It is noted that the SFDR was increased by almost 7 dB from 64.84 dB, in case of applying index-matching fluid at both input and output crystal ends, to 71.83 dB in case of index-matching fluid applied only at input

end. Table 5.6 summarizes the linearity test results with various temperatures on sample # 21. ΔT in Table 5.6 is the range of temperature which yields a linear region on the plot in Figure 5.7. According to results, the smaller this value is the better SFDR.

The SFDRs at a modulation depth of 8.36% were also measured to compare with the theoretical SFDR value of 23.6 dB for this modulation depth with no feedback. The highest SFDR of 33.2 dB, 9.6 dB above the aforementioned theoretical value, was obtained with index-matching fluid only at the input end and T = 37.67ºC.

Results for an 8 µm channel waveguide on the same sample (# 21), given in Table 5.7, are similar to those for the 7 µm waveguide in Table 5.6.

Table 5.6 Values of SFDR for various conditions and temperatures on sample # 21

Temperature (°C)	ΔT (°C) for linear region	Index-matching fluid applied conditions	$SFDR_2$ (dB)	$SFDR_3$ (dB)	$SFDR_3$ (dB) at 8.36% mod. depth
23.31 (room temp)	-	Both ends	64.84	68.04	27.94
		None	71.07	69.17	30.57
		Input only	70.22	68.04	29.07
30.30	0.244	Both ends	66.40	68.31	28.86
		None	72.36	70.38	31.25
		Input only	71.27	69.86	30.28
31.67	0.349	Both ends	65.36	68.21	28.84
		None	71.28	69.76	30.49
		Input only	71.08	69.16	30.50
37.67	0.209	Both ends	67.27	70.02	31.19
		None	72.15	71.49	32.72
		Input only	73.35	71.83	33.20

Table 5.7 Summary SFDR test of sample # 21 on an 8 µm wide channel waveguide

Condition of Sample Ends	Temp. (°C)	ΔT for linear region	SFDR$_2$ (dB)	SFDR$_3$ (dB)	SFDR$_3$ (dB) at 8.36% mod. depth
Index-matching fluid applied at both ends	23.31	-	64.20	67.00	28.08
	30.96	0.206	66.59	68.51	31.02
	34.10	0.378	65.07	67.46	28.38
Air at both ends	23.31	-	69.36	69.77	30.06
	30.96	0.206	71.51	70.87	31.26
	34.10	0.378	69.81	69.46	30.28
Index-matching fluid at input end	23.31	-	70.02	69.16	29.43
	30.96	0.206	72.04	70.98	32.82
	34.10	0.378	69.61	68.96	30.46

Other samples were tested in the same manner as the previous sample (# 21). Sample # 17 was modulated with the same frequency and parameters as previous sample on its 7 µm wide single mode channel waveguide. The result summary shown on Table 5.8 is similar to previous sample. The SFDR was improved from the worst case by nearly 7 dB.

Table 5.8 Summary SFDR test of sample # 17 on a 7 μm wide channel waveguide

Condition of Sample Ends	Temp. (°C)	ΔT for linear region	SFDR$_2$ (dB)	SFDR$_3$ (dB)	SFDR$_3$ (dB) at 8.36% mod. depth
Index-matching fluid applied at both ends	23.31	-	63.32	67.43	27.15
	30.33	0.179	66.17	69.87	30.88
	37.04	0.358	63.52	67.84	28.49
Air at both ends	23.31	-	70.63	69.93	28.68
	30.33	0.179	71.33	70.33	31.24
	37.04	0.358	70.28	69.77	29.29
Index-matching fluid at input end	23.31	-	67.89	66.63	27.65
	30.33	0.179	71.07	70.12	32.39
	37.04	0.358	69.25	68.75	29.63

The waveguide with a width of 7 μm in sample # 18 was also tested to determine SFDRs. When index-matching fluid was applied to both crystal ends, the substrate modulated at room temperature gave an SFDR of 65.73, limited by second harmonic nonlinearity. Whereas, when the fluid was applied only at the input end of the substrate and the modulation was done at 30.21°C, the SFDR increased to 72.37 dB, limited by the third harmonic. Again, the SFDR was improved from the worst case by nearly 7 dB. Test results on this waveguide are shown in Table 5.9.

Table 5.9 Summary SFDR test of sample # 18 on a 7 μm wide channel waveguide

Condition of Sample Ends	Temp. (°C)	ΔT for linear region	SFDR$_2$ (dB)	SFDR$_3$ (dB)	SFDR$_3$ (dB) at 8.36% mod. depth
Index-matching fluid applied at both ends	23.31	-	65.73	69.07	27.68
	30.21	0.248	68.92	71.03	30.68
	38.01	0.578	66.22	69.85	28.93
Air at both ends	23.31	-	70.53	69.28	29.14
	30.21	0.248	72.13	71.33	32.23
	38.01	0.578	70.32	69.58	30.68
Index-matching fluid at input end	23.31	-	72.01	71.62	29.80
	30.21	0.248	73.83	72.37	33.19
	38.01	0.578	72.17	71.38	30.83

CHAPTER VI

CONCLUSIONS

The use of optical feedback for improving the response linearity of an electrooptic light modulator has been demonstrated. The modulator is configured as a straight channel waveguide flanked by electrodes in a lithium niobate (LiNbO$_3$) substrate. Light is coupled into the waveguide in both TE and TM polarizations, and a voltage applied across the electrodes causes a relative phase shift between these two polarization components. A linear polarizer at the output converts the phase modulation to intensity modulation. Optical feedback of light in the TE and TM modes results from reflection of light at the polished edges of the substrate.

Channel waveguides supporting a single guided mode for both TE and TM polarizations were produced by diffusing 1,040-1,100 Å thick Ti films at temperatures of 1,025°C to 1,035°C into a LiNbO$_3$ substrate. The waveguides and modulators were characterized at a wavelength of 1.55 μm using a distributed feedback (DFB) laser. Insertion losses of 3.01 dB for TE polarization and 3.16 dB for TM polarization were achieved on 7 μm wide channel waveguide.

The modulators were driven with a sinusoidal voltage waveform. A modulation depth of 98.5% was achieved on a device with a 7 μm wide channel waveguide. To minimize harmonics of the modulating frequency in the intensity output, the magnitude of the optical feedback and the substrate temperature were adjusted. The feedback level was altered by applying refractive index-matching liquid

to one or both ends of the waveguide at the edges of the crystal. It was found that a high degree of response linearity in the presence of feedback was achievable at certain substrate temperatures.

The spurious-free dynamic range (SFDR) relative to the noise floor was measured under different conditions in an effort to maximize the modulator response linearity. An SFDR of 68.04 dB, limited by third-order nonlinearity, was achieved by applying index-matching fluid to the input end of the substrate. This compares with an SFDR of 64.84 dB limited by second-order nonlinearity when index-matching fluid was applied at both ends of the substrate. By changing the temperature of the same substrate to adjust the phase shifts experienced by TE and TM polarizations, the SFDR with index-matching fluid at the input end increased to 71.83 dB, limited by third-order nonlinearity.

In tests at constant modulation depth, an improvement of as much as 9.6 dB in SFDR vs. the theoretical value for an interferometric modulator without feedback was achieved.

These results indicate that optical feedback is an important factor in the response linearity of electrooptic modulators of the type investigated, and that adjusting the feedback level and substrate temperature can be used to optimize the modulator performance.

CHAPTER VII

SUGGESTIONS FOR FUTURE WORK

Based on the modulator linearity test results, an improvement in linear dynamic range is achievable by adjusting the optical feedback level and the phase shift experienced by TE and TM polarization modes. The Fresnel reflection plays vital part in optical feedback. In order to obtain wider linear dynamic range, a dielectric film of a material such as SiO_2 may be deposited on one or both of the crystal edges to reduce or increase the optical feedback shown in Figure 7.1.
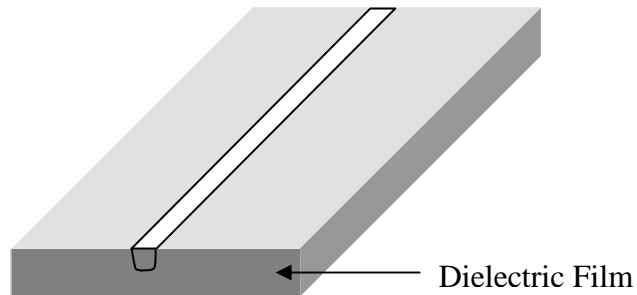
Dielectric Film

Figure 7.1 Dielectric film applied to the input edge of the substrate to adjust the reflectance

By choosing dielectric materials with different refractive indices, and varying the thickness of each material, it is possible to adjust the level of optical feedback over a wide range, from a small fraction of 1% to > 20 % per end of the substrate. The dielectric film can be applied by e-beam evaporation or magnetron-sputtering method.

Furthermore, the substrate length can be changed in order to adjust the values of the single pass amplitude loss coefficients, which would also affect modulator response characteristics.

REFERENCES

[1]   C. Laliew, X. Zhang, and A. Gopinath, "Linearized optical directional-coupler modulators for analog RF/microwave transmission systems," *IEEE Microwave Theory and Techniques Digest*, pp. 1829-1832, 2000.

[2]   W. B. Bridges and J. H. Schaffner, "Distortion in linearized electrooptic modulators," *IEEE Trans. Microwave Theory Tech.*, vol.43, no. 9, pp. 2184-2197, Sept. 1995.

[3]   S. K. Korotky and R. M. De Ridder, "Dual parallel modulation achemes for low-distortion analog optical transmission," *IEEE J. Select. Areas Commun.*, vol. 8, no. 7, pp. 1377-1381, Sept. 1990.

[4]   D. J. M. Sabido IX, M. Tabara, T. K. Fong, C. Lu, and L. G. Kazovsky, "Improving the dynamic range of a coherent AM analog optical link using a cascaded linearized modulator," *IEEE Photon. Technol. Lett.*, vol. 7, no. 7, pp.813-815, Jul. 1995.

[5]   Y. W. Boulic, "A linearized optical modulator for reducing third-order intermodulation distortion," *J. Lightwave Technol.*, vol. 10, no. 8., pp. 1066-1070, Aug. 1992.

[6]   L.M. Johnson and H.V. Roussell, "Linearization of an interferometric modulator at microwave frequencies by polarization mixing," *IEEE Photon. Technol. Lett.*, vol. 2, no. 11, pp. 810-811, Nov. 1990.

[7] M. L. Farwell, Z. Lin, E. Wooten, and W. S. C. Chang, "An electrooptic intensity modulator with improved linearity," *IEEE Photon. Technol. Lett.*, vol. 3, no. 9, pp. 792-795, Sept. 1991.

[8] S. A. Hamilton, D. R. Yankelevich, A. Knoesen, R. T. Weverka, and R. A. Hill, "Comparison of an in-line asymmetric directional coupler modulator with distributed optical loss to other linearized electrooptic modulators," *IEEE Trans. Microwave Theory Tech.*, vol. 47, no. 7, pp. 1184-1193, Jul. 1999.

[9] L. Zhang, P. Myslinski, J. Chrostowski, H. Hua, O. Berolo, J. Lee, and F. Harlow, "Ten GHz MMIC predistortion circuit for improved dynamic range of broadband analog fiber-optic link," *Microwave Opt. Technol. Lett.*, vol. 11, no. 6, pp. 293-295, 1996.

[10] A. Yariv, *Optical Electronics in Modern Communications*, 5th edition. New York: Oxford, 1997.

[11] H. Nishihara, M. Haruna, and T. Suhara, *Optical Integrated Circuits*. New York: McGraw-Hill, 1989.

[12] J. Singh, *Optoelectronics, An introduction to Materials and Devices*, International edition. New York: McGraw Hill, 1996.

[13] E. H. Turner, "High-frequency electrooptic coefficients of lithium niobate and lithium tantalate," *IEEE J. Quantum Electron.*, vol. 2, no. 4, pp. 128, Apr. 1966.

[14] I. Savatinova, S. Tonchev, R. Todorov, M. N. Armenise, V. M. N. Passaro, and C. C. Ziling, "Electro-optic effect in proton exchanged $LiNbO_3$ and $LiTaO_3$ waveguides," *J. Lightwave Technol.*, vol. 14, no. 3, pp. 403-409, Mar. 1996.

[15] R. C. Alferness, "Waveguide electrooptic modulators," *IEEE Trans. Microwave Theory Tech.*, vol. MTT-30, no. 8, pp. 1121-1137, Aug. 1982.

[16] T. K. Fong, M. Tabara, D. J. M. Sabido IX, and L. G. Kazovsky, "Dynamic range of externally modulated analog optical links: optical amplification versus coherent detection," *IEEE Photon. Technol. Lett.*, vol. 6, no. 2, pp. 270-272, Feb. 1994.

[17] J. H. Schnaffner, J. F. Lam, C. J. Gaeta, G. L. Tangonan, R. L. Joyce, M. L. Farwell, and W. S. C. Chang, " Spur-free dynamic range measurements of a fiber optic link with traveling wave linearized directional coupler modulators," *IEEE Photon. Technol. Lett.*, vol. 6, no. 2, pp. 273-275, Feb. 1994.

[18] G. E. Betts, "A linearized modulator for high performance bandpass optical analog links," *IEEE Microwave Theory and Techniques Digest*, pp. 1097-1100, 1994.

[19] P. E. Green, Jr., *Fiber Optic Networks*. Englewood Cliffs, NJ: Prentice Hall, 1993.

[20] Z. Tang, "Study of utilizing static photoelastic effect in intergrated optical devices," Ph.D. Dissertation, Texas A&M University, Department of Electrical Engineering, College Station, Texas, 1994.

[21] J. L. Jackel, V. Ramaswamy, and S. P. Lyman, "Elimination of out-diffused surface guiding in titanium-difused $LiNbO_3$," *Appl. Phys. Lett.*, vol. 38, pp. 509-511, Apr. 1981.

[22] T. Tamir, *Guided-Wave Optoelectronics*. Berlin, Germany: Spring-Verleg, 1988.

[23] E. L. Wooten, K. M. Kissa, A. Yi-Yan,. E. J. Murphy, D. A. Lafaw, P. F. Hallemeier, D. Maack, D. V. Attanasio, D. J. Fritz, G. J. McBrien, and D. E. Bossi, "A review of lithium niobate modulators for fiber-optic communications systems," *IEEE J. Select. Topics in Quantum Electron.*, vol. 6, no.1, pp. 69-82, Jan./Feb. 2000.

[24] W. K. Burns and G. B. Hocker, "End fire coupling between optical fibers and diffused channel waveguides," *Appl. Opt.*, vol. 16, pp. 2048-2049, 1977.

[25] P. C. Becker, N. A. Olsson, and J. R. Simpson, *Erbium-doped Fiber Amplifiers; Fundamental and Technology*. San Diego, CA: Academic Press, 1999.

[26] G. Eisenstein, and S. K. Korotky, "Antireflection coatings on lithium niobate waveguide devices using electron beam evaporated yttrium oxide," *Elect. Lett.* vol. 21, no. 9, pp. 363-364, Apr. 1985.

APPENDIX 1

FABRICATION OUTLINE OF ELECTROOPTIC LIGHT MODULATOR

1. Cut an *x*-cut, *y*-propagation $LiNbO_3$ wafer into small substrates.

2. Clean substrates with proper solutions.

3. Deposit Ti Film on the substrates with DC sputtering machine.

4. Delineate channel waveguide pattern by a positive photolithography process.

5. Hard bake and O_2 descum the substrates.

6. Etch Ti layer by using Reactive Ion Etching (RIE).

7. Wet etch to remove the remaining Ti using HF acid.

8. Diffuse Ti channel waveguide film into substrates.

9. Polish both ends of substrates.

10. Delineate electrode pattern by an image reversal process or a negative photolithography.

11. Deposit the layers of metal: Cr, Al, and Au using electron beam evaporation.

12. Lift off the unwanted metal

APPENDIX 2

CUTTING SUBSTRATES WITH DICING SAW

1. Mount the tape to an O-ring and stick $LiNbO_3$ wafer onto the tape.

2. Turn on 4 knobs/switches for saw: air knob (black); vacuum pump power switch (silver); vacuum line switch (black); water line valve (yellow).

3. Measure resistance between blade and spindle. The meter should read less than 1 or 2 kΩ.

4. **R** Turn on saw power (big red button).

5. Select program # 300 and check parameters: Mode 30, Speed = 0.127 mm/s, 25,000 rpm.

6. For 1 mm thick wafer, Height = 0.6 mm. and Thickness = 1.2 mm.

7. Clean chuck with methanol and Q-tip.

8. **R** Turn program off and turn spindle on and wait for stable.

9. Zero chuck (be prepared to press RESET if blade cuts into chuck).

10. Press ALIGN; align stage/sample with crosshairs using panel on the right.

11. Align the substrate with crosshairs and make a test cut on the tape.

12. To cut, press SINGLE CUT.

13. When finished, do steps marked **R** in reverse order to shut down the system

14. In any emergency cases, push RESET to shut down the system

APPENDIX 3

SUBSTRATE CLEANING PROCEDURE

1. Gently brush with Q-tip using soapy water.

2. Rinse thoroughly with D.I. water.

3. Sonicate in acetone for 10 minutes.

4. Rinse thoroughly with methanol.

5. Sonicate in methanol for 10 minutes.

6. Rinse thoroughly with D.I. water.

7. Sonicate in soap water for 10 minutes.

8. Rinse thoroughly with D.I. water.

9. Sonicate in D.I. water for 10 minutes.

10. Gently brush with Q-tip using methanol if needed.

11. Blow dry with N_2.

APPENDIX 4

DC SPUTTERING PROCESS

1. Vent the chamber then load the samples.

2. Close the chamber and turn on mechanical pump on the back.

3. Turn on Chamber Roughing Valve and wait until the pressure is below 50 µm of mercury.

4. Close Chamber Roughing Valve and slowly open high vacuum valve all the way.

5. Wait until the pressure goes below 2×10^{-6} µm of mercury.

6. Flow Ar gas at the rate of 140 sccm.

7. Adjust high vacuum valve to make Hastings vacuum gauge reads 20 µm of mercury.

8. Turn on DC power supply, push the red button, and turn the current knob slowly to 40 mA.

9. Pre-sputter for 15 minutes. (check if current is 40 mA)

10. Moving the plate to a desired position to start depositing Ti on the substrates.

11. After finishing deposition, slowly move current knob to zero position, and turn off DC power supply.

12. Close LEAK valve and turn off Ar gas flow switches, and close Ar gas duel.

13. Wait for more than 2 hours to let the system cool down before taking substrates out of the chamber.

APPENDIX 5

POSITIVE PHOTOLITHOGRAPHY PROCESS

1. Dehydrate the substrate in the oven set at 135ºC for 10 minutes. Take out from the oven and let it cool down for at least 10 minutes.

2. Spin Clariant photoresist AZ5214 for 30 sec at 5,000 rpm.

3. Soft back for 2 minutes at 100ºC and let it cool down.

4. Expose a substrate with UV light intensity of 21.3 mW/cm^3 with pattern mask for 3 seconds without filter.

5. Develop the substrate in the solution of Shipley MF312:H_2O in a ratio of 1:1.2 for 45-50 seconds, then rinse with DI water for 3 minutes.

6. Softly blow dry the substrate with Nitrogen.

APPENDIX 6

O$_2$ PLASMA ASHING (BARREL ASHER)

1. Turn on power supply and vacuum pump.

2. Set the temperature of the chamber to 135ºC, and wait until it reaches to that temperature.

3. Vent and load the substrate into the chamber.

4. Pump chamber and O$_2$ line down to a pressure of 50 µm of Mercury.

5. When the temperature reaches 130ºC, establish O$_2$ flow so that the chamber pressure is 500 µm of Mercury.

6. Tune forward RF power to 100 W while keeping reflected RF power below 5 W.

7. Set timer for 5 minutes.

8. When finish, vent the system and take out the substrate.

9. Set the temperature setting to 0ºC.

10. Turn off vacuum pump and power supply.

APPENDIX 7

REACTIVE ION ETCHING (RIE)

1. Turn on the main power and turn on a mechanical pump.

2. Turn on the cooling-water system, and set the temperature to 35°C. Let it warm up for 15-20 minutes.

3. Vent the chamber

4. Load the substrate into the chamber.

5. Close the chamber, and open a roughing valve while pushing the door tightly closed.

6. When the pressure shows below 7,000 µm Mercury, close a roughing valve, and open a high vacuum valve.

7. Turn on a blower, and wait until the pressure drops to 20 µm Mercury or below.

8. Flow Ar, CHF_3, and He into the chamber with flow rates of Ar = 3, He = 7.5, and $CHF_3 = 30$.

9. Change the flow switch to AUTO, wait until the pressure indicator shows 70 and the gas flow rates stabilize.

10. Turn on RF power, adjust forward power to 350 mW and reflected power below 0 mW.

11. Start etching and timing.

12. When finish etching, turn off RF power, close all gas valves and switches. Wait for 2 minutes.

13. Close high vacuum valve, turn off Baratron and blower, vent chamber, and take out substrates.

APPENDIX 8

WET ETCH

1. Put the substrate in diluted acid (HF:DI water = 1:20) for 8-10 seconds depending on Ti thickness.

2. Put the substrate in water for a minute.

3. Gently blow the substrate with Nitrogen.

APPENDIX 9

TITANIUM IN-DIFFUSION PROCESS

1. Load well cleaned substrates onto alumina (AL_2O_3) holder, and put the holder in the center of big alumina tube.

2. Use glass rod to push alumina tube to the center of quartz tube.

3. Seal tube with quartz cap at front and connect to bubbler.

4. Turn on compressed air and adjust airflow at the back of a furnace.

5. Adjust settings for desired temperature.

6. Wait until the airflow stabilizes at 1 bubble/second, then turn on control switch.

7. Wait until current meter stabilizes, then turn on element switch.

8. Wait until the furnace temperature reaches to a desired temperature. It takes about 45-60 minutes.

9. When current meter starts to swing on/off, begin counting diffusion time.

10. Keep bubbling rate at 1 bubble/second throughout the process.

11. After completion of the diffusion, turn off element and control switches.

12. After 3-4 hours, the temperature should drop below 200ºC, close gas and remove the quartz cap at the front.

13. After the furnace temperature drops to room temperature, take out the substrate.

APPENDIX 10

POLISHING PROCESS

1. Apply one small drop of U.V. cure epoxy (Norland optical adhesive P/N 8101) to the substrate waveguide surface.

2. Place another substrate on top of the first one, so that both waveguide surfaces face each other.

3. Expose the pair to U.V. light for 10 minutes at each end to cure epoxy.

4. Secure mount to polishing fixture.

5. Mix 0.5 teaspoon of polishing grit with lapping oil and spread mixture evenly over the rough polishing plate.

6. Polish at speed of 6 rpm for 10-15 minutes.(Rough polishing)

7. Unfasten mounting fixture from polishing fixture and clean.

8. Mix 3 μm diamond polishing grit with water, soap, and suspendex following the mixing formula.

9. Pour the solution into polishing wheel and tray.

10. Put polishing jig onto the plate.

11. Turn on pump to circulate slurry mixture.

12. Polish for about 50-60 minutes with the speed of 18 rpm.

13. Clean substrate and inspect the edges under microscope before moving on.

14. Clean all equipments thouroughly.

15. Repeat fine polishing procedure with 0.3 µm diamond polishing grit for 45 minutes at 16 rpm.

16. Clean and Inspect edge quality under microscope. If needed, repeat polishing.

17. Clean all equipment thoroughly.

18. Soak substrate into MF312 until separation.

19. Clean substrate with methanol and water.

20. Inspect edge quality and cleanness under microscope prior to optical testing.

APPENDIX 11

IMAGE REVERSAL PROCESS

(NEGATIVE PHOTOLITHOGRAPHY PROCESS)

1. Dehydrate the substrate in the oven set at 135ºC for 10 minutes. Take out and let it cool down.

2. Apply photoresist on the substrate, and spin at 5,000 rpm for 30 seconds.

3. Soft bake the substrate at 96ºC for 1 minute. Let it cool down.

4. Expose the U.V. light of the intensity 21.3 mW/cm^2 onto the substrate with mask without filter for 3 seconds.

5. Soft bake again at 106ºC for 2 minutes. Let it cool down.

6. Flood expose with U.V. light of the intensity 21.3 mW/cm^2 with filter for 2 minutes.

7. Develop the substrate with the solution of MF312:H_2O (1:1.2) for 30-40 seconds, then put the substrate into D.I. water for 3 minutes.

8. Gently blow dry with nitrogen.

APPENDIX 12

E-BEAM PROCEDURE

1. Clean the plate with sand-blasting gun.

2. Check the nitrogen tank if it is enough for a run.

3. Mount substrate onto the plate.

4. Test the thickness monitor. If working properly, the light should brink twice.

5. Flip on the control and make sure that roughing valve and Hi-vacuum valve are closed.

6. Turn on vent switch to vent the chamber.

7. Load substrates and metals in the system.

8. Close the lid and turn on mechanical pump and open roughing valve.

9. Turn on ionization gauge to monitor the pressure.

10. Pump the system until the pressure shows below 70 µm of Mercury.

11. Close the roughing valve and open Hi-vacuum valve.

12. Pump the system until the pressure is below 5×10^{-6} Torr.

13. Turn on thickness monitor.

14. Set the keyboard switch to Program, and set Control PWR to Auto.

15. Set density, Z-ratio, and tooling.

16. Reset the keyboard switch to Lock and reset Control PWR to Main Power.

17. Press ZERO button.
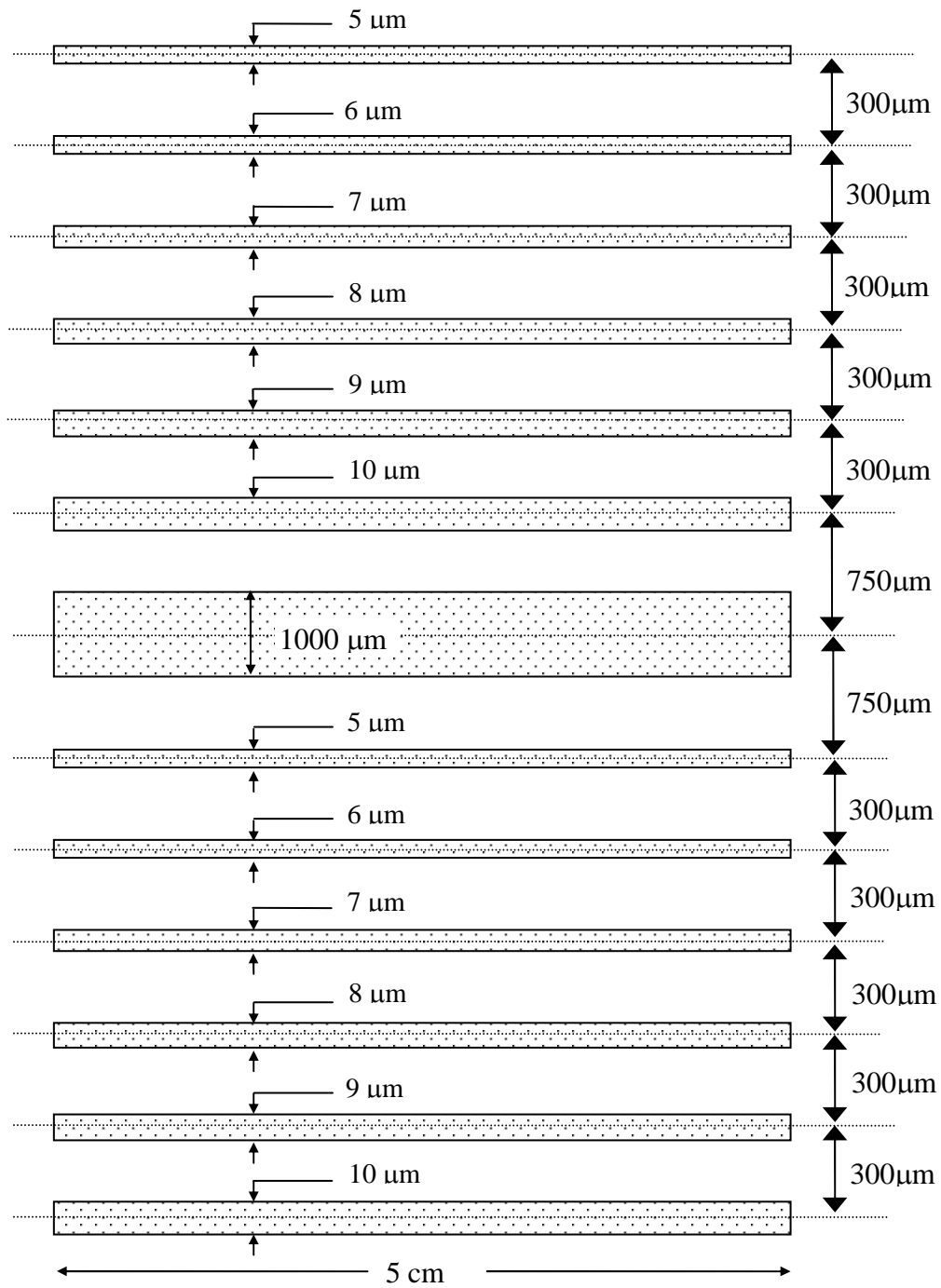
18. Turn on cooling water system.

19. Plug in the key.

20. Turn on main power, and wait for the system to start.

21. Press the High Voltage ON button, and wait for relay to turn on (click).

22. If current shows, turn off High Voltage immediately. Short circuit is presented.

23. Turn on the scanner.

24. Wait for the beam to warm up.

25. Increase the current gradually, and adjust the light spot position to start deposition.

26. Rotate the crucible if needing to deposit more than one.

27. After finish, turn down the current and voltage. Plug off the key.

28. Turn off the thickness monitor.

29. Turn off the ionization gauge.

30. Wait for 5 minutes, and turn off the power supply.

31. Wait for 15 minutes, close cooling water for crystal, and turn off crystal cooler.

32. Wait for 45 minutes, and close other cooling water under the front panel.

33. Turn off Hi-vacuum switch.

34. Vent the system, and take out samples.

35. Once everything has been removed from the chamber, rough slightly.

36. Turn off control.

APPENDIX 13

LIFT-OFF PROCESS
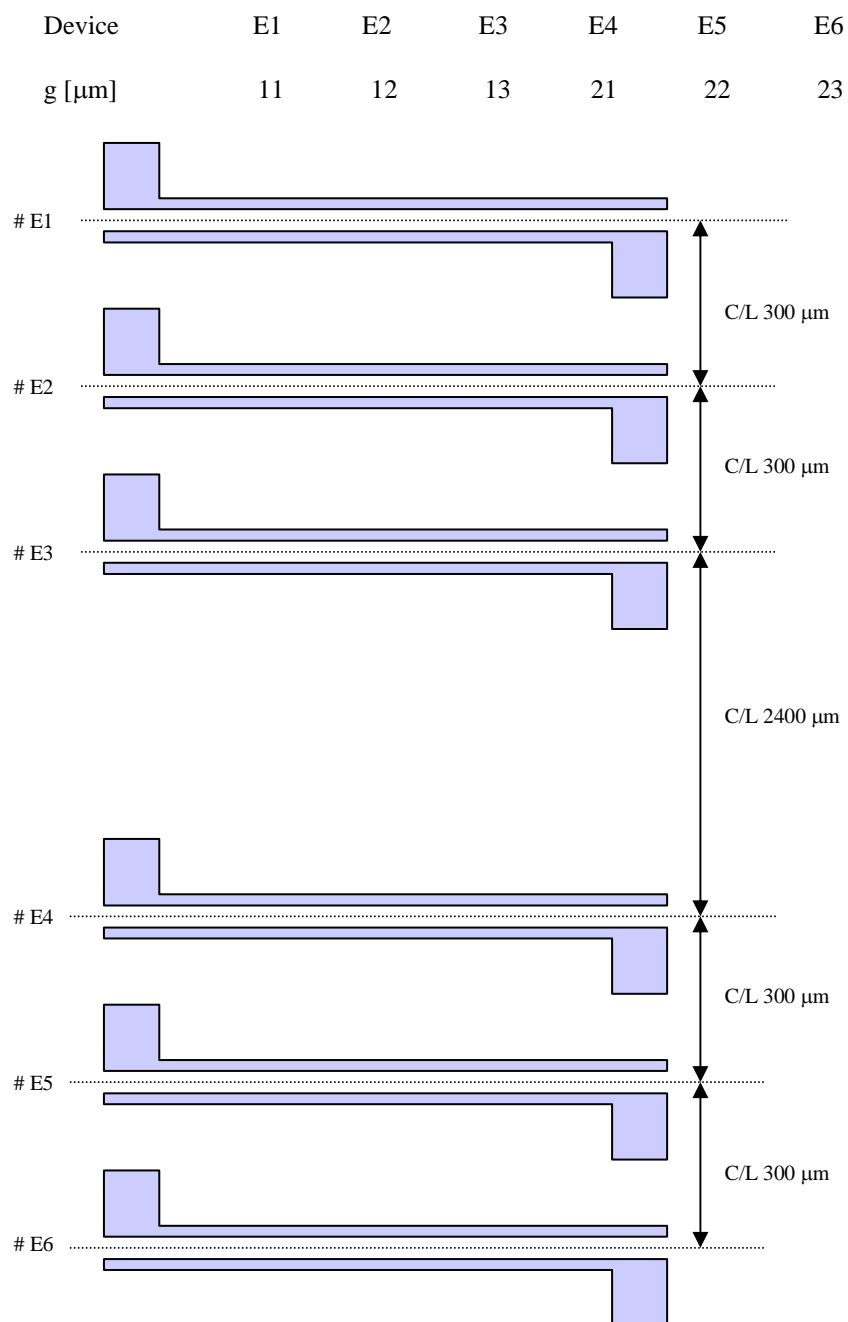
1. Place the substrate on the sample holder.

2. Sonicate in acetone until the unwanted portions of metals are peeled off.

3. Gently clean the sample prior to optical testing.

APPENDIX 14

CHANNEL WAVEGUIDE LAYOUT

5 um

6 um

7 um

8 um

9 um

10 um

1000 um

5 um

6 um

7 um

8 um

9 um

10 um

300μm

300μm

300μm

300μm

300μm

750μm

750μm

300μm

300μm

300μm

300μm

300μm

5 cm

APPENDIX 15

MASK LAYOUT OF ELECTRODES

Device		E1	E2	E3	E4	E5	E6
g [μm]		11	12	13	21	22	23

E1

E2

C/L 300 μm

E3

C/L 300 μm

C/L 2400 μm

E4

C/L 300 μm

E5

C/L 300 μm

E6

APPPENDIX 16

SCHEMATIC DRAWING OF ELECTRODE
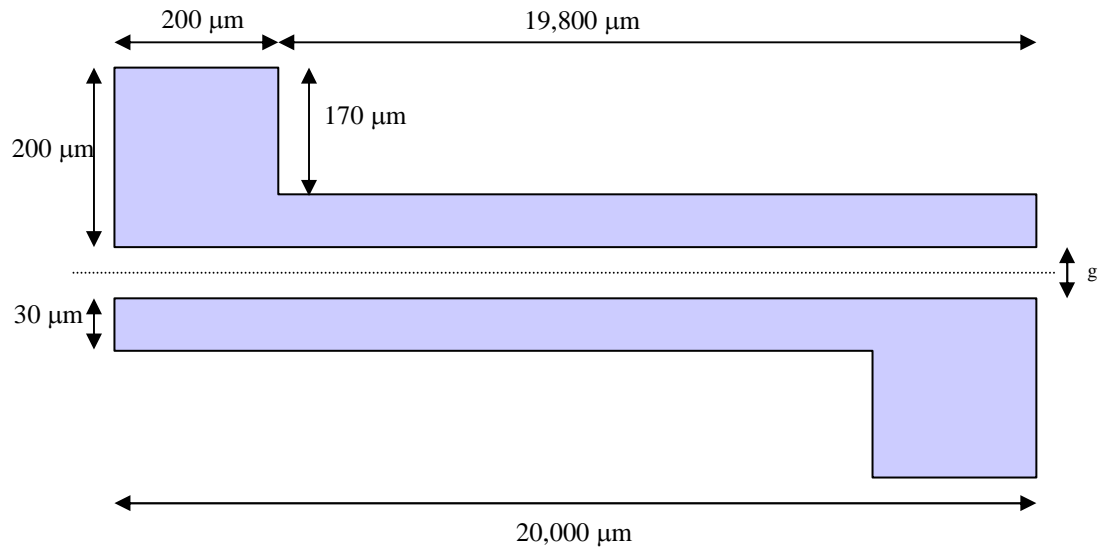
APPENDIX 17

SFDR ANALYSIS OF MZ INTERFEROMETRIC MODULATOR

In Mach-Zehnder interferometric electrooptic modulator, the transmittance is a sinusoidal function of the voltage-induced optical phase shift. With a quadrature biasing, the signal photocurrent I_s can be written as

$$I_s = I_0(1 + \sin\phi) \tag{a17.1}$$

where I_0 is the average photocurrent and ϕ is the induced phase shift that depends on the modulating voltage. A sine function of equation (a17.1) is expanded, so that equation (a17.1) can be rewritten as

$$I_s = I_0\left(1 + \phi - \frac{\phi^3}{6} + \frac{\phi^5}{120} - \dots\right) \tag{a17.2}$$

If the modulator is driven by a single-frequency voltage waveform of

$$\phi = A\cos(\omega t) \tag{a17.3}$$

where A is the modulation amplitude and $\omega = 2\pi f$ with f being the modulation frequency. An equation (a17.3) can be rewritten as

$$\phi = A\left(\frac{e^{i\omega t} + e^{-i\omega t}}{2}\right) \tag{a17.4}$$

The electrical power that is generated in the load resistor with a resistance R at the fundamental frequency f is given by

$$P_{s1} = \frac{RI_0^2 A^2}{2} \tag{a17.5}$$

The third harmonic power P_{s3} can be given by

$$P_{s3} = R\left(\frac{I_0\phi^3}{6}\right)^2 = \frac{RI_0^2A^6}{1152} \tag{a17.6}$$

where the photodetector noise power P_n is expressed as

$$P_n = 2eRI_0B \tag{a17.7}$$

with e an electron charge and B the receiver bandwidth. By solving for A that makes the third harmonic power in equation (a17.6) equals to the noise power in equation (a17.7), it yields

$$A = 3.24\left(\frac{2eB}{I_0}\right)^{\frac{1}{6}} \tag{a17.8}$$

The spurious-free dynamic range SFDR$_3$, defined as P_{s1}/P_n using the value of A from equation (a17.8), is calculated from equation (a17.5) and (a17.7) to be

$$\text{SFDR}_3 = 3.30\left(\frac{I_0}{eB}\right)^{\frac{2}{3}} \tag{a17.9}$$

For biasing exactly at quadrature, only odd harmonics are present in the receiver output. However, a slight bias error can result in sizable even harmonics. From equation (a17.1), if we have a bias error, ϕ_e, the photocurrent, I_s, can be written as

$$I_s = I_0(1 + \sin\phi') \tag{a17.10}$$

with $\phi' = \theta_e + \phi$. Assume $\theta_e \ll 1$, I_s can be expanded as

$$I_s = I_0\left(1 + \phi_e + \phi - \frac{\phi_e\phi^2}{2}\right) \tag{a17.11}$$

The second harmonic power P_{s2} is given by

$$P_{s2} = \frac{RI^2\phi_e^2 A^4}{16}$$ (a17.12)

and it equals to the noise power when

$$A = 2\left(\frac{2eB}{I_0\phi_e^2}\right)^{\frac{1}{4}}$$ (a17.13)

Thus, the SFDR$_2$ (P_{s3}/ P_n), calculated using A from equation (a17.13), becomes

$$\mathrm{SFDR}_2 = \frac{2}{\phi_e}\sqrt{\frac{I_0}{2eB}}$$ (a17.14)

APPENDIX 18

MATLAB PROGRAM FOR CALCULATING SFDR

```
clear;
format short;
e_charge = 1.602e-19;
dV = 1e-2;                % delta V
theta_in = pi/4;
theta_out = pi/4;
r13 = 8.6e-12; r33 = 30.8e-12;
k = r13/r33;
I0 = 8.73e-5;            % Photocurrent
B = 1.25e6;             % Bandwidth
RR(1) = 0.131;              % Rx
RR(2) = 0.143;              % Ry
phi(1) = 0;            % phi(x)
phi(2) = pi/2;            % phi(y)
del(1) = .136;              % power attenuation(x)
del(2) = .143;              % power attenuation(y)
Vmin = -3*dV;
Vmax = 3*dV;
V = Vmin - 0.0000001;
i = 1;
while V <= Vmax
   for j=1:2
      R = RR(j);
      if j == 1
         kth = cos(theta_in);
```

```
        fac = 1;
        att = exp(-del(1));
      else
        kth = sin(theta_in);
        fac = k;
        att = exp(-del(2));
      end
      att2 = att^2;
      ph = phi(j)+fac*V;
      den = 1+(R^2)*(att2*att2)+2*R*att2*cos(2*ph);
      Ar(j)=(1-R)*att*(1+R*att2)*cos(ph)*kth/den;
      Ai(j)=(1-R)*att*(1-R*att2)*sin(ph)*kth/den;
    end
    Br = Ar(1)*cos(theta_out)+Ar(2)*sin(theta_out);
    Bi = Ai(1)*cos(theta_out)+Ai(2)*sin(theta_out);
    sm(i) = (Br^2)+(Bi^2);
    V = V+dV;
    i = i+1;
end
    kfit = I0/(e_charge*B);
    for i = 1:3
      jp = i+4;
      jm = -i+4;
      ss(i+1)=0.5*(sm(jp)+sm(jm));
      dd(i+1)=0.5*(sm(jp)-sm(jm));
    end

    ss(1) = sm(4);
    dd(1) = 0;
```

```
cc(1) = ss(1);
cc(2) = (45*dd(2)+dd(4)-9*dd(3))/(30*dV);
cc(3) = (270*ss(2)+2*ss(4)-27*ss(3)-245*ss(1))/(180*(dV^2));
cc(4) = (13*dd(2)+dd(4)-8*dd(3))/(-24*(dV^3));
cc(5) = (39*ss(2)+ss(4)-12*ss(3)-28*ss(1))/(-72*(dV^4));
cc(6) = (dd(4)-cc(2)*3*dV-cc(4)*27*(dV^3))/(243*(dV^5));
cc(7) = (ss(4)-cc(1)-cc(3)*9*(dV^2)-cc(5)*81*(dV^4))/(729*(dV^6));


cx = cc(2)^2;


DR(1) = (cc(2)/cc(1))^2;
DR(2) = (cx/cc(3))*sqrt(kfit);


DR(3) = ((abs(kfit/cc(4)))^(2/3))*cx;
DR(4) = (kfit^(3/4))*cx*0.5/(sqrt(abs(cc(5))));
DR(5) = (kfit^(4/5))*cx*0.525/((abs(cc(6)))^(2/5));
DR(6) = (kfit^(5/6))*cx*0.405/((abs(cc(7)))^(1/3));



SFDR = DR(2:6);
SFDR = 10*log10(abs(SFDR))

end
```

VITA

Apichai Bhatranand was born in Bangkok, Thailand in 1975. He received a B.S. degree in electrical engineering from Mahidol University, Thailand in 1995. Upon his arrival to Texas A&M University in 1996, he worked as an engineer at Bewcon Company, Ltd. in Bangkok, Thailand. He received an M.E. degree in electrical engineering from Texas A&M University in 1998. In the same year, he continued graduate work to pursue Ph.D. degree in electrical engineering at Texas A&M University. He can be reached at the following address:

Apichai Bhatranand

235 Soi 5 Seri 6 Rd.

Suanluang, Bangkok 10250

Thailand